Politecnico di Torino

Collegio di Ingegneria Elettronica, Fisica
e delle Telecomunicazioni

Corso di Laurea Magistrale
in Ingegneria Elettronica

Tesi di Laurea Magistrale

Integration of a Custom Designed Microfabricated Sensor Chip into Hanging-Drop Networks for Microtissues Analysis

Relatori:
Prof. Danilo Demarchi
Prof. Andreas Hierlemann

Candidato:
Massimiliano Gusmaroli

Settembre 2018

Abstract

Microfluidic technology is gaining popularity in building cell-culture systems. These platforms allow to set up a more physiological relevant environment when compared to static devices, which features flow control and interconnection of multiple cell or tissue types. In the context of microfluidic platforms, a novel system involving an open reconfigurable hanging-drop network for microtissue aggregation and culturing has been proposed by the Hierlemann group at the Bio Engineering laboratory of ETH Zurich. Here, cell suspension are formed, and the cells sediment by gravity force at the liquid-air interface forming microtissues. Drops can be easily connected together with microfluidic channels enabling the analysis of different spheroids interaction.

An integrated electrical sensing system would be beneficial to these microfabricated devices, being able to enhance the analysis obtained by visual inspection with an electrical characterization of the sample. For example, analysis methods based on Electrical Impedance Spectroscopy (EIS) have been proven to provide reliable biological information from cell culture experiments.

This thesis presents the design and fabrication of a test device based on the integration of a Micro-Electrodes Array (MEA), developed by the Hierlemann group, with a microfluidic hanging-drop platform for spheroid cell culture. The aim of this test device is to analyze the feasibility of the fabrication process, while verifying the working principle for the EIS based detection. In this framework, custom designed chips with different layouts were designed and fabricated, and then assembled with a hanging-drop network. The stability of the system under continuous perfusion was investigated and verified. Moreover, by means of EIS, this test device was proven to effectively provide spheroid-size related information.

Acknowledgments

I would first like to thank my thesis advisor Prof. Danilo Demarchi of Politecnico di Torino, and my supervisors at ETH Zurich Prof. Andreas Hierlemann, Dr. Vijay Viswam, Dr. Mario Modena and Raziyeh Bounik. Their passionate help and participation have been fundamental during the development of this work.

I would also like to thank all the people of the Bio Engineering Laboratory at the Bio Systems Science and Engineering department. I am grateful to all of you for having me in your group and for backing me up during my stay.

I must express my very profound gratitude to my family and my closer friends. Your unfailing support and continuous encouragement endlessly inspired me throughout the last five years.

Finally, I wish to thank Alessandra. This accomplishment would not have been possible without your love and your confidence.

Thank you.

Contents

Abstract i

Acknowledgments ii

Contents iii

List of figures v

List of tables vii

1 Introduction 1

1.1 3D Cell cultures . . . 2
1.2 Hanging drop network . . . 4
1.3 Electrical Impedance Spectroscopy . . . 7
1.4 Micro Electrode Array systems . . . 12
1.5 State of The Art . . . 14
1.6 Thesis outline . . . 15

2 COMSOL simulations 16

2.1 Geometry and materials . . . 16
2.2 Physics and study . . . 19
2.3 Simulation results . . . 20

3 Microfabrication 25

3.1 Microfluidic platform . . . 26
3.2 Silicon Chips . . . 28
3.3 Glass PCB . . . 33
3.4 Assembly . . . 37

4 Experimental data 41

4.1 Loading and perfusion . . . 41
4.2 Electronic readout system . . . 42
4.3 Microscope setup . . . 44

4.4 Stability of medium conductivity 45
4.5 Sensitivity and electrode-sample distance 47

5 Discussion **52**

6 Conclusion and Outlook **54**

Bibliography **55**

List of Figures

1.1 2D to spheroid cultures transition. 3
1.2 Microfluidics for cell cultures. 4
1.3 A simple microfluidic hanging drop network. 5
1.4 Zoom on single drop 5
1.5 Radius and height correlation in drops. 6
1.6 A simple equivalent circuit of a cell and its frequency response. . . . 7
1.7 Frequency response of impedance for a muscle tissue 8
1.8 Equivalent circuit of an electrode in an electrolytic medium 10
1.9 Double layer capacitance 10
1.10 HD-MEA Chip 13

2.1 3D model of the sensing region. 17
2.2 Comparison between the two chip layouts 17
2.3 Computed electric field lines and voltage distribution in electrolyte medium 21
2.4 Computed electrode size dependence 22
2.5 Computed impedance frequency response 23
2.6 Computed drop height dependence of sensitivity 23
2.7 Computed electrode size dependence with rims 24

3.1 Device components 25
3.2 Microfluidic platform 26
3.3 Schematic view of the microfluidics 27
3.4 Microfluidics fabrication steps 28
3.5 Common dimensions for each chip 29
3.6 Sensing electrodes 29
3.7 Masks for chips design 31
3.8 PCB layout. 33
3.9 Scheme of the microfabrication process 36
3.10 Device assembly steps 37
3.11 Ball-ball bonding 39
3.12 Device pictures at different stages 40

4.1 Principle scheme of a generic Lock-in filter 43
4.2 Scheme of a transimpedance amplifier circuit 43
4.3 Experiment: stability of the medium conductivity 46
4.4 Experiment: sensitivity of the electrodes, frequency response 48
4.5 Experiment: sensitivity of the electrodes at 100 kHz 49

List of Tables

2.1 Table of dimensions in simulation. 18

2.2 Table of materials properties. 19

2.3 Table of physical properties. 20

3.1 Table of chip dimensions. 31

3.2 Table of PCB dimensions. 34

1

Introduction

Cell cultures can be considered an indispensable field of study in many different areas, both in research and industry. The very first established cell line, HeLa, derived in 1951 from Henrietta Lacks, consisted in the first time that human cells were grown in a laboratory. Being "immortal", in the sense that they were not going to die after a certain number of divisions, they turned out to be a keystone in scientific research, allowing to conduct many medical experiments that were not possible before. Then, steps forward have been achieved thanks to the breakthroughs in DNA profiling and analysis, allowing to identify many others cell lines. Concerning mammalian cell cultures, these advancements were combined with new culturing methods and media supplements, with more flexibility to experimental variations. Another relevant improvement was given by 3D culturing, which offers a physiological environment closer to *in vivo* conditions: the capability of culturing three dimensional clusters of cells has allowed to obtain a better representation of the biological dynamics that happen in a real *in vivo* organism when compared to a monolayer culture (Ravi et al., 2015). These 3D models are more effective in realistically translate research results to in vivo tests, due to the smaller gap to the actual physiology of a living being, enabling the analysis of more complex interactions. First papers about 3D culturing were published in the late 60s, with no significant improvements until 1992 (Ravi et al., 2015). Then the number of papers increased gradually, becoming exponential after 2000. Now around 6000 results can be obtained when searching for "3D cell cultures" in PubMed database[1]. Despite the huge advancements achieved in the past years, still limited methods have been developed to provide real-time and integrated monitoring solutions in 3D systems.

[1]Verified at 10/09/2018.

Optical characterization of the tissue is still the most common analysis method for these kind of culturing, even though this process has limited throughput.

Microfluidics is gaining popularity as tool for realizing novel culture systems, being able to provide a more physiologically relevant micro-environment: some of the possible benefits are flow control, dynamic stimuli of the sample and interconnections of several tissue cultures. Furthermore, microfluidics can be integrated with custom micro-fabricated electrodes, setting up a heterogeneous measure system. This solution would combine the advantages in 3D cell culturing given by a microfluidic platform with a non invasive and continuous electrical analysis of the tissue and the surrounding environment. In particular, sensing methods based on Electrical Impedance Spectroscopy (EIS) have been proven to be useful in many single cell analysis (Alexander et al., 2013; Haandbæk et al., 2014; Zhu et al., 2012) and also for microtissues (Misun et al., 2017; Schmid et al., 2016; Bürgel et al., 2016). Merging in a single device a microfluidic based technology for cell culturing with the EIS sensing approach will be the main subject of the work described hereafter.

1.1 3D Cell cultures

Most of the research activities into cells data extraction and their analysis up to about 10 years ago has been based on monolayer cultures, assuming that these cultures were effectively replicating the physiology of real *in vivo* tissues. Actually, this has been proven to be a wrong assumption, since the environment in which cells can grow in real organisms is different from the one supporting these cell layers (Pampaloni et al., 2007). For example, the biochemistry of the cell-cell interaction or the placement dependent mechanisms can not be replicated in such simplified systems (Ravi et al., 2015).

In particular, the communication network between multiple cells or tissues plays a key role in the life cycle of a cell: cells multiplication, apoptosis and migration are strongly influenced by the environment, and these effects underline the importance of 3D cell culture systems. For example, the migration speed of cells

has been proven to be determined differently in 2D and 3D structures (Pampaloni et al., 2007) . When cells are placed on planar surfaces their migration speed only depends on their adhesiveness, while when they are part of a 3D matrix they move depending on more complex parameters such as mechanical properties and arrangement in space. Due to these effects of surrounding environment on the cell life cycle, also the gene expression can be different when comparing 2D and 3D cell arrangements (Bissell et al., 1982). Hence, since these events are lost in 2D cultures, they can not be sufficiently predictive when it comes to drug testing. Relevant recapitulation of the tissue physiology in cell cultures is needed for more reliable drug-screening tests, and a better rate of success during clinical trials in pharmaceutical research is a key point for the companies involved.

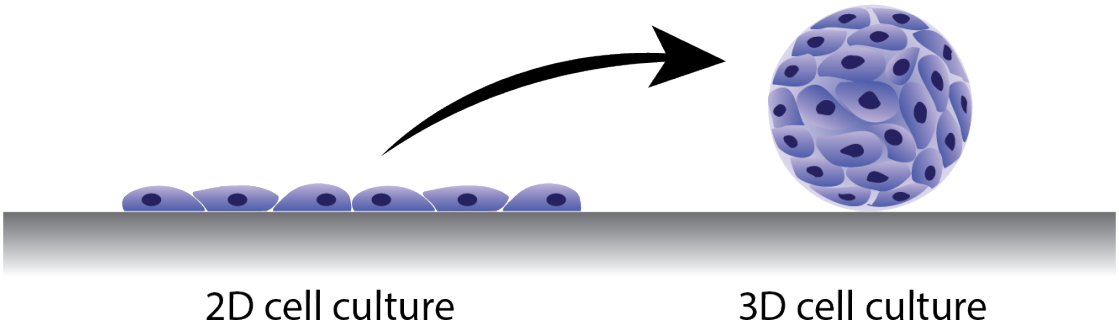

Figure 1.1: 2D to spheroid cultures transition.

This forces to move research from monolayer cultures to other approaches closer to the physiology of living beings, such as 3D multicellular aggregates (Fig. 1.1). In particular, the main interest of this work is oriented towards cellular spheroids, defined as a scaffold-free multicellular aggregate with a spherical-like shape which is not adherent to any substrate. This kind of aggregates can exploit the trend of many different cells to join together and build a single cluster. By using spheroids, many different tissues have been replicated, such as cartilage (Jukes et al., 2008), pancreatic (Lumelsky, 2001) and cardiac (Kehat et al., 2001), and also organs were formed, like pituitary gland (Suga et al., 2011), cortical tissue (Eiraku et al., 2008) and optic cup (Eiraku et al., 2011).

1.2 Hanging drop network

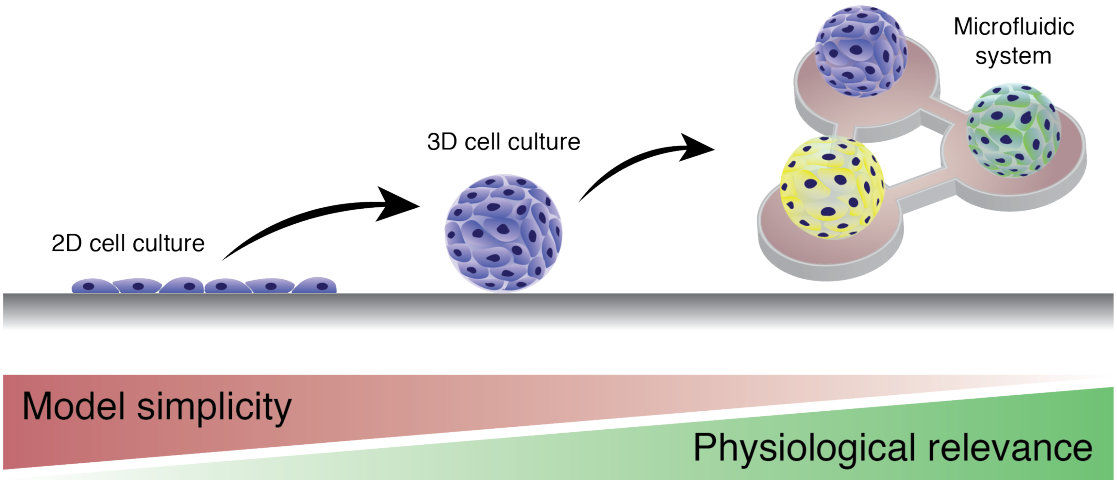

Figure 1.2: Microfluidics for cell cultures.

Biological applications of microfluidics are becoming more and more popular thanks to the high control of fluid flow. Microchannels, flow mixers, valves and pumps can be important features when it comes to high precision manipulation and analysis of single cells or microtissues. Therefore, a step further the spheroid culturing can be its integration into a microfluidic platform. This is a first step towards a comprehensive structure, which can replicate biological networks in a larger scale. Furthermore, microfabricated systems capability of culturing different samples connected in a network is the basis for the idea of body-on-a-chip. Such devices enable for *in vitro* replication of complex multi organ interaction by imitating the *in vivo* blood-mediated interaction. This can be achieved through inter tissue communication, respecting a physiologically relevant order.

In this framework, hanging drop technology offers advantages compared to other microfluidic system. This technique is based on an open platform of one or eventually many wells connected together, which can be filled with liquid and operated in upside-down position (Fig. 1.3). This allows the formation of droplets, used as culturing environments. Due to the increase of the surface to volume ratio when scaling down dimensions, these drops exhibit good stability over time thanks to surface tension. External hydrophobic rims can be designed to delimit wet regions

and improve stability (Hsiao et al., 2012) (Fig. 1.4).

Figure 1.3: A simple microfluidic hanging drop network.

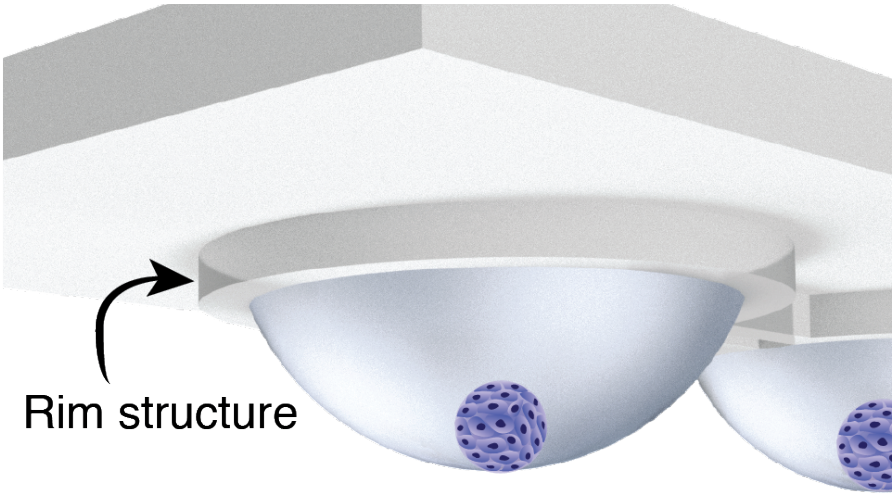

Figure 1.4: Zoom on single drop.

As previously mentioned, in such small systems surface forces are prevalent to volume forces such as gravity. The spherical-cap shape of the drop is mainly induced by the liquid surface tension, while its internal pressure is directly related to its size. Young-Laplace equation relates the relative internal pressure with drop radius:

$$\Delta p = \frac{2\gamma}{r} \tag{1.1}$$

where γ is the specific surface tension (N/m). Moreover, the radius of the spherical cap decreases with the growth of the drop, starting from infinite when the drop is

flat down to the radius of the well when the drop is filled at its maximum. Then, interconnected drops exhibit the capability of self adjust their size, since bigger drops are connected to a higher internal pressure and vice versa.

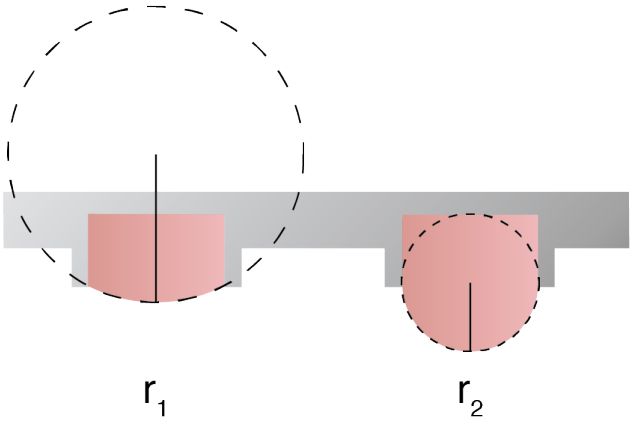

Figure 1.5: Radius and height correlation in drops.

One relevant advantage of this technology is the capability to form multicellular microtissues directly into the platform. Cells are inserted in each drop and, simply by gravity force, sediment at the bottom of the drop. In this way, cells do not interact with solid surfaces, where they can adhere and spread. The round shape of the drop promotes the interaction of cells, which can then aggregate and form scaffold free spheroids. Therefore, the formed microtissue lays on the liquid-air contact surface, where can be easily accessed. Another advantage of an open microfluidic technology is related to the enhanced O_2-CO_2 exchange between medium and surrounding atmosphere, which represents a problem in closed platforms. Moreover, bubble-related issues during the filling process are absent in such device.

1.3 Electrical Impedance Spectroscopy

The ability of reliably monitoring the growth of cellular culture and the parameters related to the surrounding environment is a key point in the field of biological and pharmaceutical research. This is commonly done by visual inspection, a procedure that might require time and bring stress to the analyzed culture, eventually generating sources of errors in the measurement process. Moreover, this method is not suitable in case real-time monitoring is required.

One possible solution is the extraction of useful physiological information from an electrical readout. In particular, a cellular environment contains both bound and free charges, respectively in the cellular membranes and in the intracellular or extracellular media. Cell membranes, mainly constituted by lipids and proteins, are mainly capacitive (around 10^{-2} F/m^2) and with very low conductivity (lower than 10^{-7} S/m) (Bertemes-Filho, 2018). On the other hand, extra- and intracellular media contain many ions and charged molecules, then their effect on the conduction is mainly resistive (around 0.5-0.6 $\Omega \cdot$ m) (Bertemes-Filho, 2018).
This complex environment can be electrically modeled with a parallel of a resistor (intra-cellular medium) and a capacitor (membranes), in series with another resistor (extra-cellular medium), giving the well known frequency response of an high pass cell (Fig. 1.6). This frequency response, uniquely defined by the values of the conductive and dielectric terms described by the complex impedance Z(ω), is then linked to the physiological parameters of the culture.

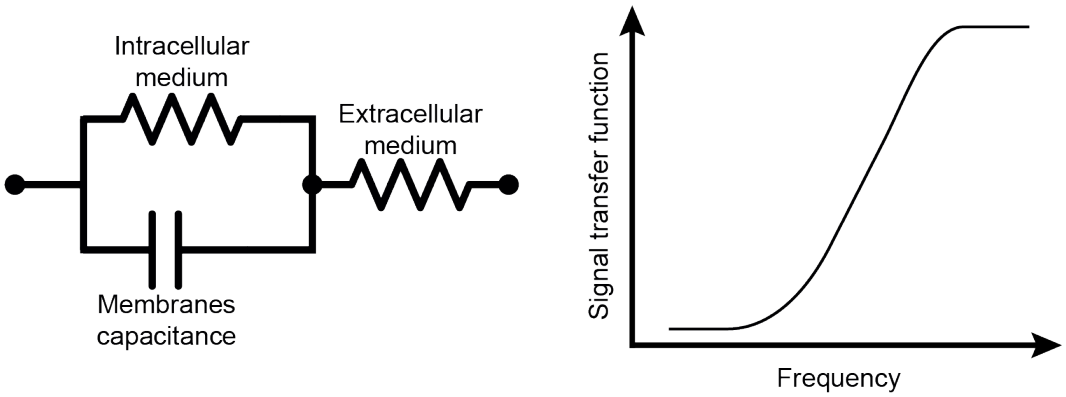

Figure 1.6: A simple equivalent circuit of a cell and its frequency response.

In a wide frequency spectrum, in the case of a multicellular tissue, the impedance modulus drops towards higher frequencies, and three major dispersion frequencies can be seen (Fig. 1.7) (Schwan and Kay, 1957; Pethig, 1987); this theoretical plot is related to a muscle tissue, but its trend is shared by other multicellular aggregates. First dispersion (α) happens at low frequency (less than 1 kHz) and its origin is non fully understood, but can be seen when dealing with multicellular aggregates (Bertemes-Filho, 2018). The second one (β) instead starts at hundreds of kHz and is related to the cellular membranes charge and discharge. Finally, the third one (γ) is due to water relaxation and takes place in the range of tens of GHz (Bertemes-Filho, 2018).

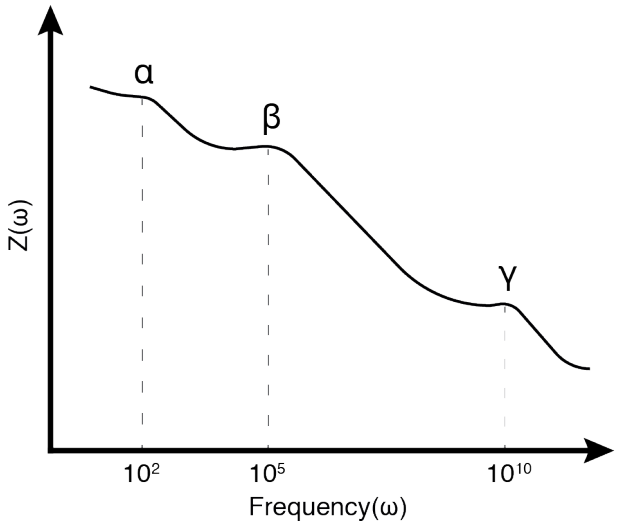

Figure 1.7: Frequency response of impedance for a muscle tissue (Schwan and Kay, 1957).

Analytically, this frequency behavior can be modeled starting from the Debye equation for a suspension of free dipoles: the complex relative dielectric permettivity of the medium, directly related to the impedance, can be estimated by:

$$\epsilon_r^* = \epsilon_{HF} + \frac{\epsilon_{LF} - \epsilon_{HF}}{1 + j\omega t} \tag{1.2}$$

where ϵ_{HF} and ϵ_{LF} are the relative permettivities at high frequency and at low

frequency (static condition) respectively.

This model was then modified (Cole and Cole, 1941), by adding an empirical dimensionless parameter α to the Debye model which helps in fitting with experimental data:

$$\epsilon_r^* = \epsilon_{HF} + \frac{\epsilon_{LF} - \epsilon_{HF}}{1 + (j\omega t)^{1-\alpha}} \tag{1.3}$$

From this complex frequency response useful physiological information can be extracted by means of Electrical Impedance Spectroscopy (EIS). This technique is based on a voltage or current stimulation over a wide frequency spectrum, followed by the recording of the electrical response of the sample. In case the stimulus is given with a wide frequency spectrum, such as a step function or a noise signal, the response is recorded in time and transformed in the frequency domain by a Fourier transform. Otherwise the stimulus can be a collection of many single harmonics and then the amplitude of the response is obtained by simply plotting them in frequency.

Electrode kinetics

The measuring setup for EIS is composed by a signal generator and an oscilloscope connected to a system of readout electrodes placed close to the biological sample, which also add resistive and capacitive terms to the global transfer function. In particular electrodes add a series electrode resistance and a series capacitance (Fig. 1.8). The first term is related to the Faradaic current, originated by electrochemical reactions at the electrode surface. The latter one is due to the progressive redistribution of the electrolyte ions, contained in the media surrounding the cell, on the electrodes surfaces, similarly to what happens in a capacitor and making the flowing current become zero after a characteristic time. This phenomenon is well known and usually referenced as *Double Layer Capacitance* (Fig. 1.9). Then, current can flow between electrode and electrolyte either by electrochemical reaction or by charge or discharge of the double layer capacitance.

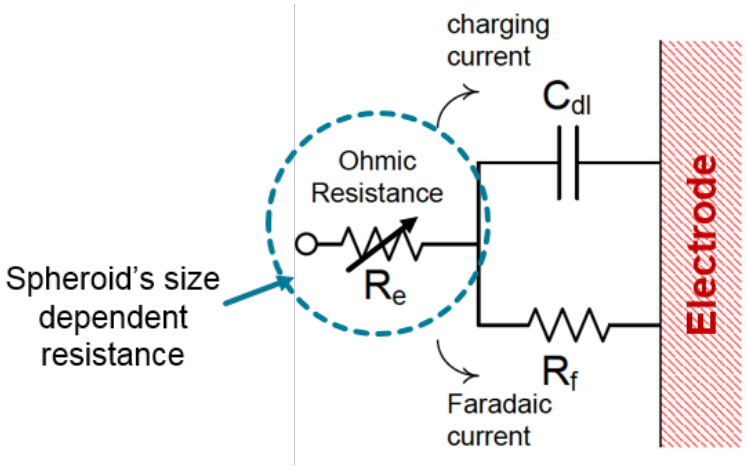

Figure 1.8: Equivalent circuit of an electrode in an electrolytic medium, plus effect of tissue.

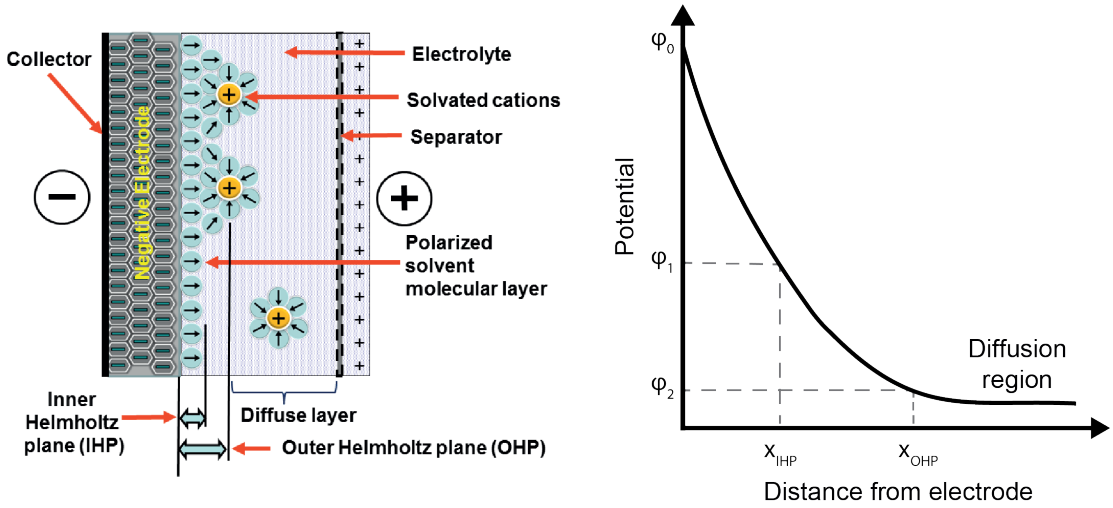

Figure 1.9: Double layer capacitance (*Wikimedia Creative Commons*) and potential distribution. ϕ_0, ϕ_1 and ϕ_2 are respectively the potential of the negative electrode surface, at the Inner Helmholtz plane (IHP, the plane passing through the adsorbed ions) and at the Outer Helmholtz plane (OHP, where the positive ions are at the closest distance to the electrode). After the OHP is located the diffusion layer.

A simplified model that takes into account the effects of the electrolyte kinetics and the redox reactions occurring in the system starts from the Butler-Volmer equation:

$$i_{loc} = i_0 \left(e^{\frac{\alpha_a F \eta}{RT}} - e^{\frac{\alpha_c F \eta}{RT}} \right) \tag{1.4}$$

where i_{loc} is the local current density[2] in the electrolyte, i_0 is the exchange current density[3], α_a and α_c are the anode and cathode reaction rates[4], F is the Faraday constant[5], η is the activation overpotential[6], R is the gas constant[7] and T the temperature.

The double layer capacitance is modeled as well, allowing to calculate the associated current summing all the current fluxes in the electrolyte. The current at the electrode-electrolyte boundary is:

$$-\mathbf{i}_s \cdot \mathbf{n} = \mathbf{i}_l \cdot \mathbf{n} = i_{DL} + \sum_m i_{loc,m} \tag{1.5}$$

where $\mathbf{i}_s$ is the current density vector at the electrode surface, equal with opposite sign to the current density vector in the electrolyte $\mathbf{i}_l$. The latter, in scalar form, is computed by summing the double layer charge and discharge current to the Faradaic currents calculated with the Butler-Volmer equation.

This model is required to correctly replicate the behavior of electrodes immersed in an electrolytic solution. The modeled terms also contribute to the measured signals, and therefore need to be taken into account during a measurment.

[2] Faradaic current (A/cm^2)

[3] Current with no electrolytic reaction (A/cm^2)

[4] Cathodic and anodic transfer coefficients, dimensionless; quantification of the portion of surface potential at the electrode-electrolyte interface that lowers the free energy barrier for the reaction

[5] 96 485.332 89 C/mol

[6] Defined as $E - E_{eq}$, electrode potential (V) minus equilibrium potential (V)

[7] 8.314 459 8 J/mol · K

1.4 Micro Electrode Array systems

Many of the chemical process constantly taking place inside and outside cells are usually connected to electrical charge displacement. In particular, cells commonly defined as electrogenic, such as cardiac or neuronal, are directly connected to a diffuse electrical activity. The study of these particular cells usually requires features such as precise stimulation and recording. Concerning extracellular electrical recording, it can be achieved by means of high density electrode arrays, on which multicellular tissues are placed (Gross et al., 1995; Stett et al., 2003). What can be obtained from these electrodes is a combined readout including electrical stimulation and recording, plus impedance measurement for EIS. These measurements are commonly obtained when the tissue lies on the electrode matrix. To obtain detailed information, very high densities are generally exploited, with a few microns pitch for the array. Moreover, measurements of electrical phenomena can be completed with chemical sensors and electrophysiological techniques (Chi et al., 2015; Guo et al., 2016), offering an heterogeneous real time detection of the whole environment.

The device this work will refer to in the following sections is a high density Micro Electrode Array (MEA), developed by the Hierlemann group at the Bio Engineering laboratory of ETH Zurich (Dragas et al., 2017), capable of multiple electrical stimulation and detection at the same time, plus electrophysiology based readouts. Furthermore, this device includes many functional units capable of on-stage postprocessing such as signal amplification, filtering and analog to digital conversion.

An integration of this device with a microfluidic platform enables new strategies in cell cultures analysis. The previously described tissue characterization obtained while the culture lays on the electrodes can be further improved with a continuous monitoring in non contact conditions. For example, combining a MEA device with the hanging drop technology allows for an EIS-based monitoring of tissue properties, plus eventually physiology dependent readouts from custom functionalized electrodes. Physiologically relevant parameters can be continuously extracted, giv-

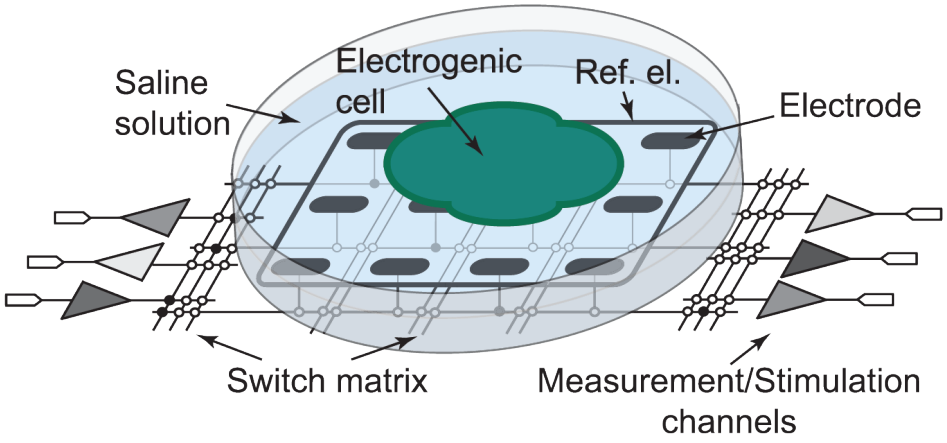

Figure 1.10: Principle scheme of the high density MEA chip developed by the Hierlemann group (adapted from Dragas et al., 2017). The sample lays above the electrodes matrix, to which stimulation or recording analog signals are applied and detected.

ing real time data and better control during the culturing process. In the meanwhile, precise electrical stimulation and recording can be done simply flipping the device and letting the tissue lay on the electrodes surface. The main benefit of this this device would be the capability of real time readout and monitoring of cell cultures which can be done directly on stage, virtually without moving the plate out the incubator as usually done for imaging. This would be an improvement, since the common microtissue spheroid formation and maintenance techniques rely on sensor-free plates, making imaging the most reliable monitoring solution. Concerning these advantages, the feature of the MEA device that will be replicated in this work is the EIS based analysis of tissue size variation, performed while the spheroid is placed in the resting position at the liquid air interface. Moreover, the test device that will be fabricated is designed to accommodate a new generation MEA chip, integrated with the previously described microfluidics.

1.5 State of The Art

By looking into the development of open microfluidics and EIS a simple road-map can be outlined from the literature, starting from hanging-drop networks and then following the steps towards the integration with electrodes for electrical sensing.

Regarding the microfluidic hanging-drop platform, an open network for multicellular spheroid aggregation and culturing has been presented previously by the Hierlemann group at the Bio Engineering laboratory of ETH Zurich (Frey et al., 2014). The features of this device are the capability of forming various multicellular microtissues and enabling interactions between them in a controlled way by the fluidic communication. This setup allows for multi-organ interaction experiments, also called body-on-a-chip experiments. On the fabrication side, the system is created through a Polydimethylsiloxane (PDMS) casting process which is then plasma bonded on a glass substrate, thus involving minimum complexity and bringing a solid culturing platform.

Then, a real time and parallel monitoring system with EIS analysis was added to a microfluidic network (Burgel et al., 2015). In this work, a multiplexed pattern of electrodes is inserted in an array of interconnected wells, in order to monitor tissue size under a continuous drug perfusion. Furthermore, these electrodes were proven to be able to follow cardiac cells beating. The setup involves an array of two-well networks and coplanar electrodes placed in the connection channels, where the spheroid is free to move. In particular, the flow is induced by gravity force on a tilting platform. Then the motion of the tissue towards and in between a couple of coplanar electrodes under a stable applied signal produces a current drop, proportional to the spheroid size.

A first work involving both hanging drops and EIS was then presented (Schmid et al., 2016). The system consists in an 8-drops network, where two couples of coplanar electrodes are placed on top. A pair of larger electrodes is proven to be sensible to drop size, while the small ones placed close to the tissue are capable of following its growth. Also in this case, it was possible to follow the beating of cardiac cells as additional information. In this device, electrodes are fabricated

on a glass slide which is inserted in a slot at the bottom of one of the wells. To enlarge the sensitivity of the measurement, the tissue is brought towards the sensing electrodes by making the drop thinner. A SU-8 trap is also inserted in the well to keep the tissue in position.

Afterwards, a multi-electrode array was integrated in a hanging drop network (Misun et al., 2017). The interconnected wells are placed on a glass substrate which contains the electrode and the routes to the readout system. A pair of additional openings are inserted in the design of the fluidic platform, in order to connect external pumps. This allows continuous perfusion and the compensation of the medium loss due to evaporation. Here the electrodes are functionalized and can be used for potentiostatic measurements.

1.6 Thesis outline

The purpose of this work is to develop a fabrication process, aimed to the integration of custom designed chips, whose dimensions are linked to the requirements of a new MEA chip, with an open microfluidic network based on the hanging drop technique. This study is intended as a proof of concept for a future integration of the new MEA chip with the hanging-drop culturing technology.

In the second chapter the preliminary analysis is shown, where Finite Element Method (FEM) simulations to investigate electrode and fluidics dimensions to enable tissue-growth detection are presented. These simulations were used to define layout geometries. In the third chapter the design of the assembled parts is presented, followed by the fabrication process and the concerning challenges that had to be faced. In the fourth chapter, experimental data about device functioning and stability is given, where microscope imaging is combined with the electrical readout of the device.

2

COMSOL simulations

The first step in the design of the device consists in simulating its physical behavior, taking into account different layout solutions. The behavior that is simulated is the one related to the previously mentioned EIS, with the final goal of obtaining an estimation of the signal that can be actually sensed. The effects due to fluid motion or concentration dependent effects have been neglected to avoid over-complicated models and because the device is meant to work in a stabilized condition, with constant perfusion of medium at very low rate. With this aim, a Finite Element Model was built in COMSOL Multiphysics (ver. 5.3a). It will be shown hereafter, focusing on the physical model of the system and how the related parameters have been selected. Simulation results are given afterwards.

2.1 Geometry and materials

The geometry that needs to be replicated is composed by a system of coplanar electrodes, contained in chips that will be described in the *Microfabrication* chapter. These coplanar electrodes are square and are implemented through two different layouts: the first one includes 4 small electrodes surrounded by two counter electrodes, which are the same in both the layouts, and separated from each other by a small gap; the latter only has one square centered electrode (Fig. 2.1). The reason of placing 4 electrodes is to evaluate the effects of off-centered electrodes with respect to the spheroid.

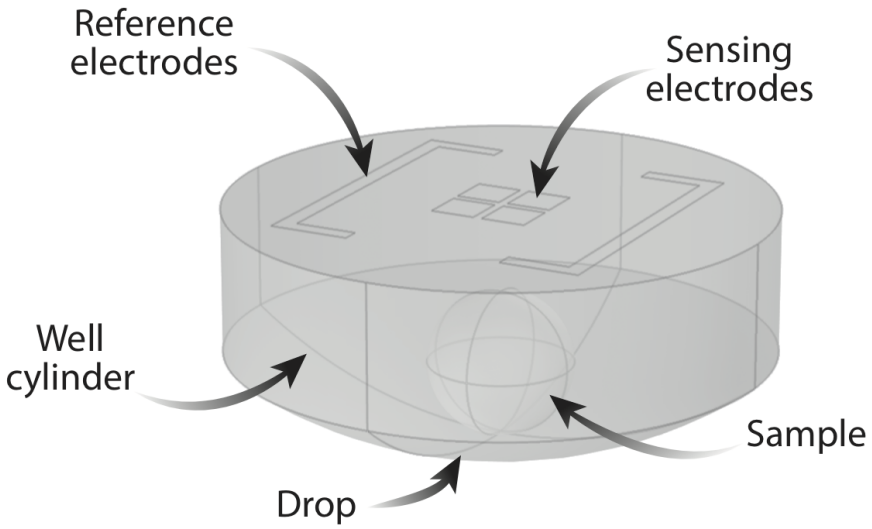

Figure 2.1: 3D model of the sensing region.

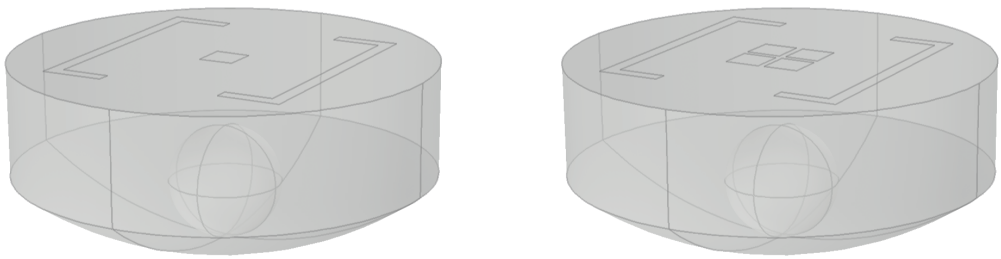

Figure 2.2: Comparison between the two geometries. Left: one single sensing electrode, Right: four sensing electrodes.

All these electrodes will be fabricated with a very thin platinum layer (200nm) if compared to the other dimensions of the structure. For this reason metal layers have been described as 2D structures, so to avoid mesh related errors. Then the plane containing the electrodes is inserted in the well, designed with a cylinder and a portion of sphere to replicate the shape of a drop hanging from a well. Finally, a spheroid is placed on the bottom of the drop to emulate the presence of a dielectric object in the medium. In particular, referring to Fig. 1.7, it can be seen how β dispersion should happen roughly at frequencies higher than 100 kHz for a muscle tissue. Actually, the involved portion of the spectrum for the β dispersion depends on the nature of the cells composing the tissue, and for commonly cultured tissues no reactive effects are expected below GHz. For this reason, the simulated effect of the tissue is essentially the one of a dielectric spheroid immersed in a conductive medium.

In the material section, the selections needing to be assigned are for the electrodes and the medium filling the drop. For the electrodes the chosen material is Platinum, from MEMS library. The material for the medium instead is added as custom material with isotropic conductivity equal to 1.2 S/m, a value that replicates the one of a common phosphate buffered solution (PBS). In the following tables dimensions and materials properties are given:

Table 2.1: Table of dimensions in simulation.

Parameter	**Value**
Counter electrodes offset from center point	800 µm
Counter electrode arms	350 µm
Counter electrode body	1800 µm
Counter electrode width	100 µm
Drop height	100 - 400 µm
Sense electrodes area	100×100 - 350×350 µm^2
Sense electrodes gap	50 µm
Recess Height	500 µm
Recess diameter	1500 µm
Tissue diameter	100 - 500 µm

Table 2.2: Table of materials properties.

Parameter	**Value**
Electrolyte electrical conductivity	1.2 S/m
Platinum electrical conductivity	$8.9 \cdot 10^6$ S/m

2.2 Physics and study

When modeling an electrode immersed in an electrolyte three physics are available, with increasing complexity:

- **Primary current distribution**: this physics only describes the Ohmic effect of the electrolyte, neglecting kinetic effects;
- **Secondary current distribution**: this physics adds to the Primary current distribution the effects of ions displacement at the interfaces;
- **Tertiary current distribution**: this physics adds to the Secondary current distribution the computation of concentration dependent terms.

Since in this model it is required to reproduce the electric response of an electrode in an electrolyte, the simulation of the kinetics effect is needed. However, since the concentration of the medium is assumed uniform and constant, the physics that includes the required features is the *Secondary current distribution*.

In the settings panel of the selected physics initial values for electrolyte potential and applied electrical potential are set to 0V. Electrodes are then marked as reference or sensing electrodes, or left insulated if disconnected. In both cases active ones are inserted as *Electrode Surfaces*, thus allowing to set the electrode reaction and double layer capacitance parameters. Electrodes electrical resistance is modeled as for a thin metal film, and no temperature dependent effect is considered. Electrode kinetics are modeled with Butler-Volmer expression from equation 1.4. The inserted values in these settings panels are given in Table 2.3, where the equilibrium potential and the exchange current density are experimentally obtained quantities (Héduit et al., 1996).

Table 2.3: Table of physical properties.

Parameter	**Value**
Metal film thickness	$0.5\,\mu m$
Electrode-electrolyte equilibrium potential[1]	$0.350 + 0.222$ V
Exchange current density	$4 \cdot 10^{-8}$ A/cm^2
Anodic transfer coefficient[2]	0.5
Cathodic transfer coefficient[2]	0.5
Double layer capacitance[3]	$0.25\,F/m^2$

[1] Equilibrium potential of Pt in PBS solution, referred to Ag-AgCl reaction potential, plus the equilibrium potential of Ag-AgCl.
[2] Transfer coefficients are approximated to 50% for high electrolyte concentration.
[3] Capacitance per unit area extracted from data in Dragas et al. (2017).

The study consists of two steps. A stationary solver is performed to solve the simulation for the unperturbed state, i.e. when no external voltage is applied. This step is then followed by a frequency domain study, where the applied signal is modeled as a perturbation of the stationary state at specific harmonics. The second study allows to find the frequency response of the system and the sensed current for each amplitude of the signal. In this study the variations in the dimensions of the geometry (Fig. 2.1) are inserted in a parametric sweep.

2.3 Simulation results

The effect that is intended to be modeled is the one shown in Fig. 2.3. Here the distribution of the electric field lines and potential changes with different tissue sizes, generating a variation in the impedance between the electrodes and then in the current flowing into them.

In the simulation results the main interest is in the current variation with different tissue sizes, that consists in the sensitivity of the device. This current is then

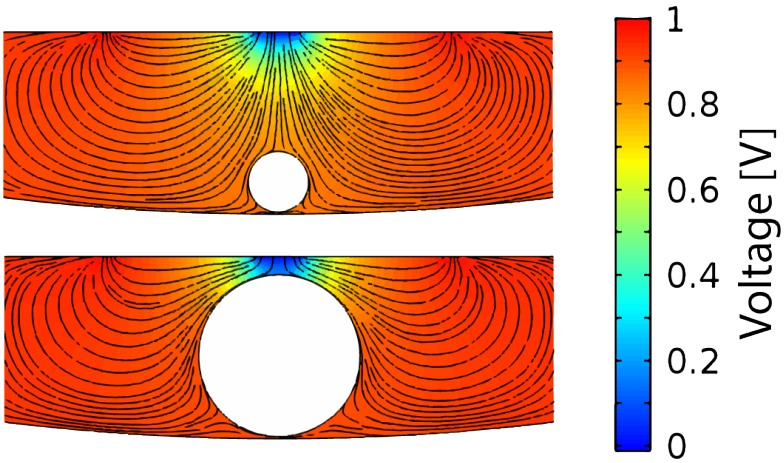

Figure 2.3: Computed electric field lines and voltage distribution in electrolyte medium for 300 µm and 800 µm tissues. Appied signal is a 1 V_{PP} sinewave at 100 kHz.

computed for several diameters of the tissue and compared for varying electrode dimensions and drop heights. What is analyzed at first is the frequency response of the system (Fig. 2.5): although the exact shorting frequency value depends on the electrode dimension, for electrodes of few hundreds of um, operating above 100 kHz allows to avoid unwanted signal attenuation due to double layer capacitance effects. In the following results the applied signal is a sinusoidal wave, 1 V_{PP}, at 100 kHz. The signal is applied on the counter electrodes, while the sensing electrode is grounded. The sensitivity is connected to the current relative variation. This is computed by integrating the normal current density vector through the surface of the counter electrodes. This is an arbitrary choice since, simulating an isolated system, the current integrated on the active sensing electrode is the same as the one integrated on the reference electrodes.

A sensitivity dependence on the sensing electrodes area can be expected. Indeed, larger sensing electrodes give a wider distribution of the electric field in the medium. This effect is illustrated in Fig. 2.4 where different electrodes sizes are considered, while the drop height is set to 100 µm. An important information from this figure is the existence of an optimal value of sensing electrode area, which eventually should be found for different layouts and tissue size. The optimal value for this configuration is 100×100 μm^2 for the four sensing electrodes and 200×200

µm^2 for the single sensing. Moreover, important remarks are the non-linearity of the function relating current and tissue size, and the range of detection starting from a diameter of 300 µm. The theoretical maximum relative variation, from 100 µm to 500 µm tissues, was then found to be around 10% for the single electrode sensing and 7-8% with four electrodes: the effect of non centering is consistent and non negligible, so spheroid movements inside the drop can affect the measurement. Furthermore, most of the variation is located in the 300-500 µm, which corresponds to the condition where the tissue is very close to the electrodes.

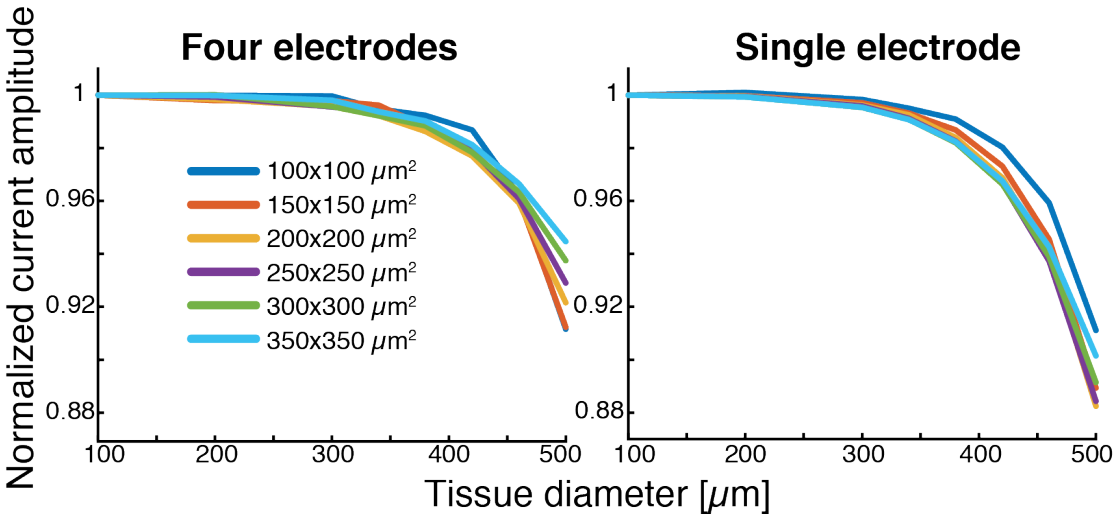

Figure 2.4: Electrode size dependence with 4 sensing electrodes and single sensing electrode. Drop height is 100 µm.

In Fig. 2.6 the effect of different drop sizes on the sensitivity is shown. It can be seen how large drops strongly reduce the detectable variation of the current with tissue size, making the sensitivity tend to zero for drops larger than 200 µm (distance from the top of the rim). This is conceivable considering that with larger drops the spheroid moves away from the sensing electrodes, thus placing far from the region of maximum density of field lines: the effect is that a lower quantity of electric field is obstructed, then the change in impedance is lower.

These first simulations are done for the ideal case, which dimensions were given

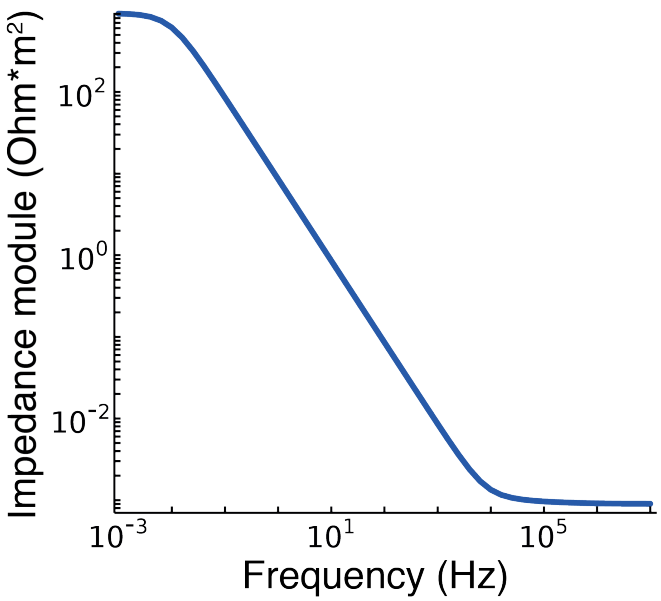

Figure 2.5: Impedance frequency response, 100um drop, 200×200 µm electrode.

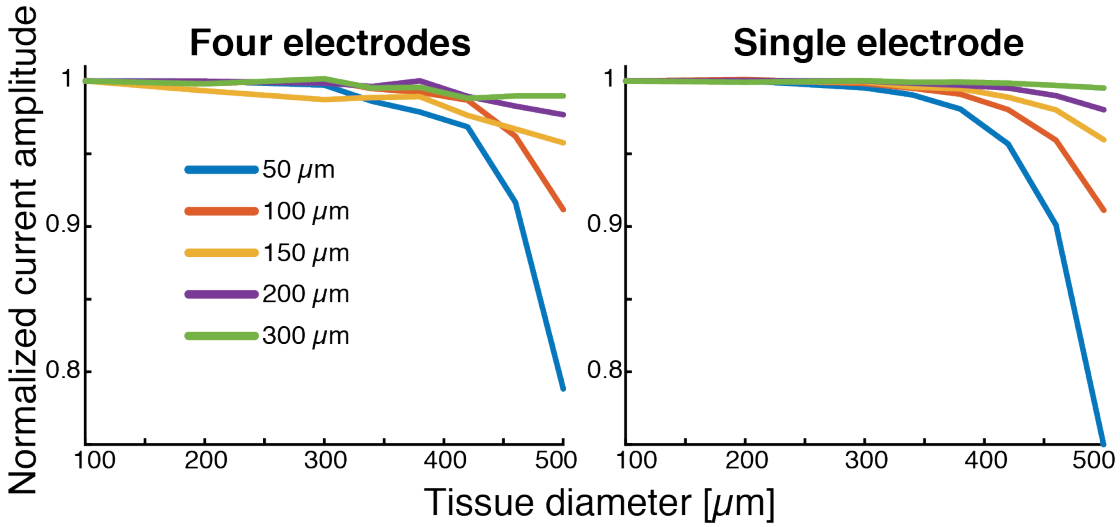

Figure 2.6: Drop height dependence of sensitivity with 4 sensing electrodes and single sensing electrode. Sensing electrode size: 150×150µm^2.

previously (Table 2.1). However, for technological reasons that will be depicted in the *Microfabrication* chapter, a further distance of 300 µm has to be added to the recess height. This has an effect on the sensitivity of the device, and this variation is shown in Fig. 2.7, where drop height is kept at 100 µm. The current variation becomes much smaller, and for tissue diameters lower than 550 µm the sensitivity is virtually zero. Concerning the optimal area for the sensing electrodes, results indicate 200×200 µm^2 for the four sensing configuration, 250×250 µm^2 for the single sensing.

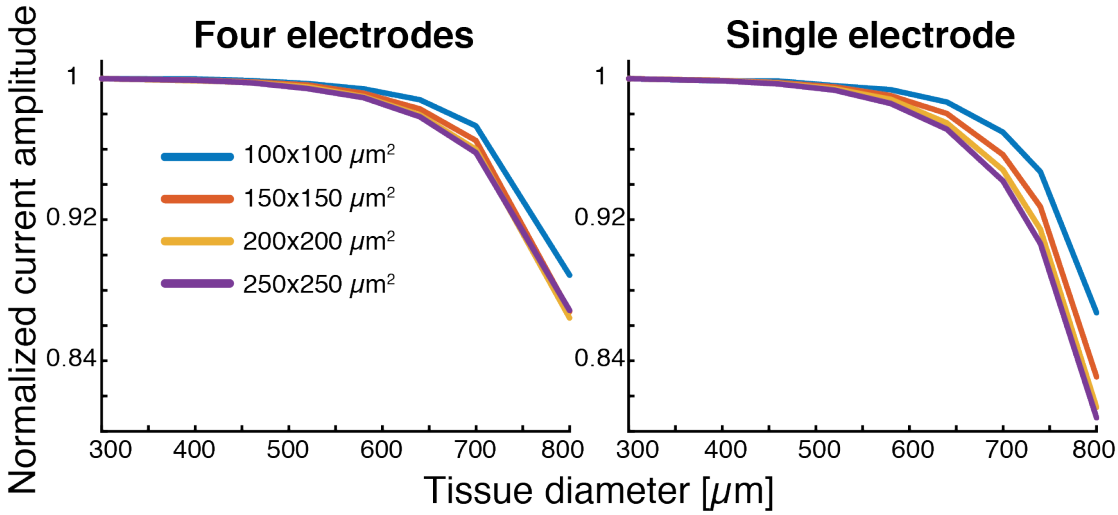

Figure 2.7: Electrode size dependence with 4 sensing electrodes and single sensing electrode, with 300 µm added to recess. Drop height is 100 µm.

3

Microfabrication

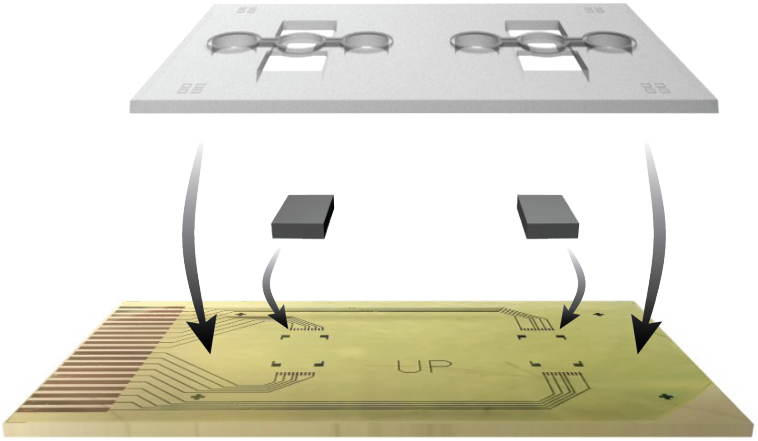

Figure 3.1: 3 main parts of the device. From top: microfluidic chip, silicon chips, glass PCB.

As previously outlined, the final goal of this work is to build a microfluidic device able to provide a robust cell culturing platform, while giving the advantage of a real-time electrical monitoring system. In this chapter the technological processes needed for the fabrication of the device will be shown. Three main components are assembled in the device (Fig. 3.1): a glass PCB substrate needed to drive the signals to the readout system, a couple of silicon chips containing the active electrodes for the EIS sensing and a microfluidic network. All of them were designed and fabricated at the department of Bio-Systems Science and Engineering of ETH Zurich.

3.1 Microfluidic platform

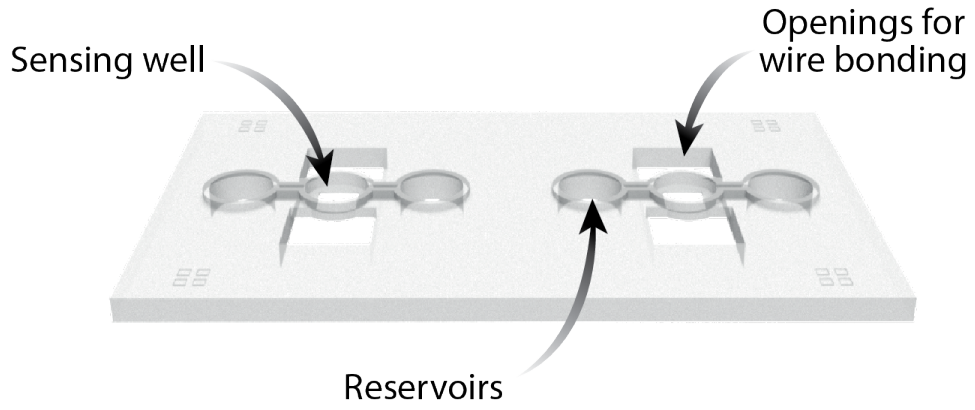

Figure 3.2: Microfluidic platform.

The microfludic structure is realized in PDMS for fast prototyping. Each fluidic chip consists of two networks composed of three wells of 3mm diameter (Fig. 3.2). Two lateral wells are necessary as reservoirs to provide additional medium to the sample, which is placed in the central one instead. The lateral wells present a height of 1300 µm, while for the central one hosting the electrodes it is 800 µm, giving respectively 9.2 µl and 5.7 µl volumes. With respect to the first design simulated in COMSOL, 300 µm rims need to be added on top of the wells to contain the drop. In this way the drop spreading around the well top can be avoided. Moreover, two additional openings are added close to the central well for the connection between the chips and the PCB.

Illustrations about the fabrication steps are given in Figure 3.4. The microfluidic system is obtained by casting PDMS (*Sylgard 184* silicone elastomer) from two 3D printed molds. These molds have been designed in Adobe Inventor 2016 and then ordered from the supplier *ProtoLabs GmbH*. The chosen material is *Accura SL 5530* with thermal post curing which gives a glass transition temperature of 122°C, suitable for PDMS curing avoiding mold reflowing. The top mold has been

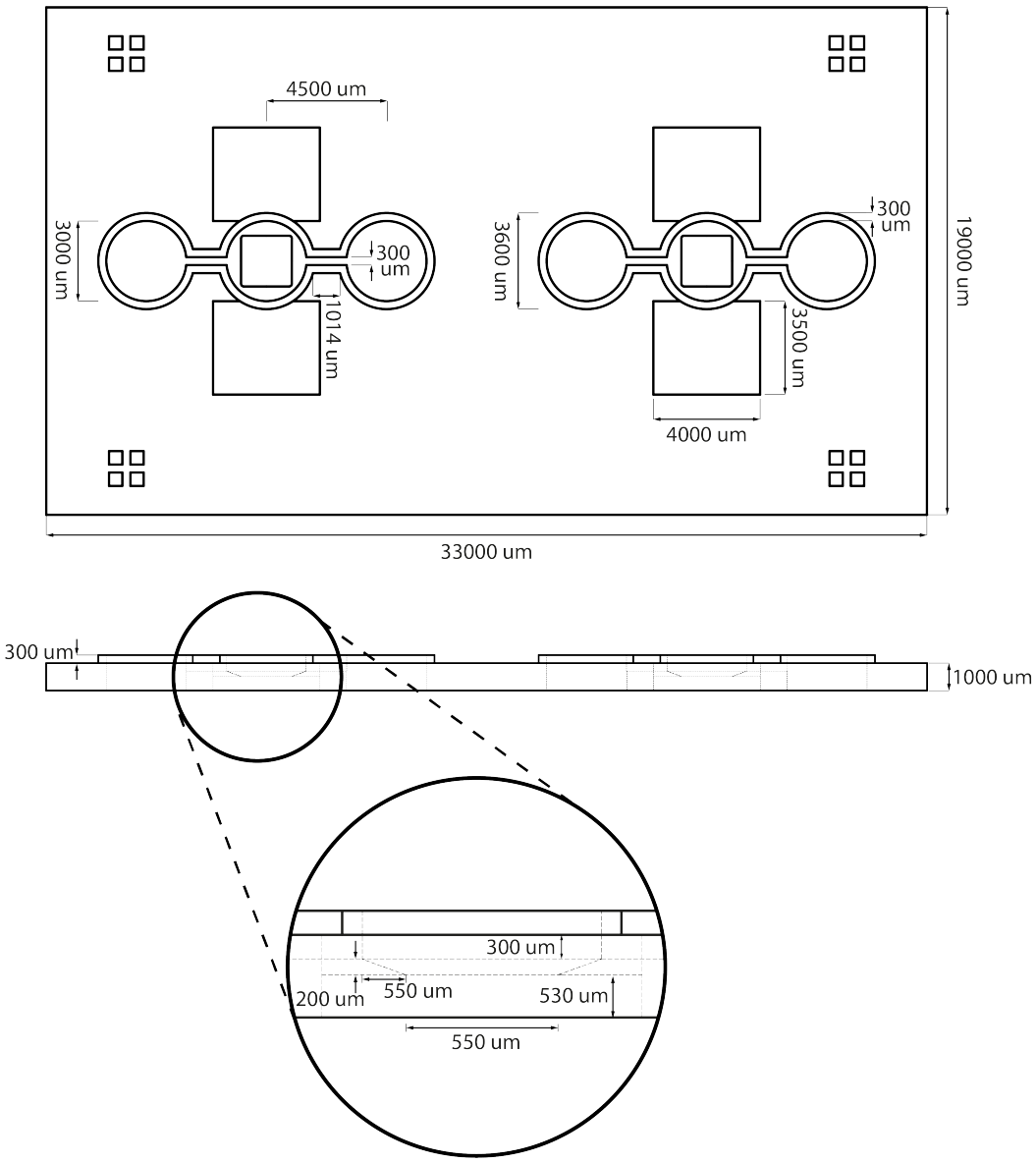

Figure 3.3: Schematic view of the microfluidics.

designed as positive image of the wanted fluidics, and from that a negative image is cast with 7:1 elastomer-curing agent ratio (degassed for 1-2 hours and cured 6 hours at 60°C) to make it stiffer and use itself as top mold for the microfluidics. The purpose of this additional step is to have a softer and flexible mold, for an easier detaching of the wanted PDMS fluidics from the molds; moreover, it is hard to obtain a good sealing in between two hard molds put in contact, while it is easy when one of the two is soft and slightly deformable. Also, to prevent PDMS-PDMS bonding, this soft mold is plasma activated (30s at 50 W, 0.4 mbar O_2) and silanized (LPCVD with 3 µl of Trichlorosilane, 30min). Then, liquid PDMS mixed in 10:1 ratio is poured in between the PDMS mold and the 3D printed bottom one, processed (degassed for 3-4 hours and cured 2 hours at 80°C) and finally detached.

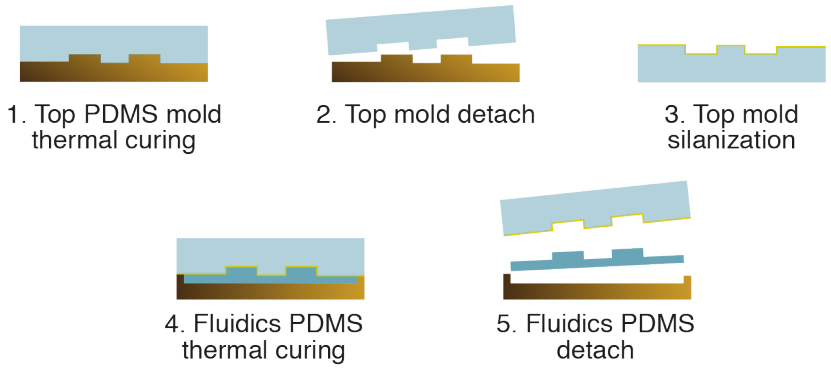

Figure 3.4: Microfluidics fabrication steps.

3.2 Silicon Chips

Platinum electrodes needed for the electrical sensing of the sample are placed on a Silicon substrate and diced in small chips, which dimensions are coherent with the ones of the full MEA chip. Each chip can provide 20 connection pads, divided on two sides, which are associated to the electrodes according to 3 different layouts. Counter electrodes position and dimensions are left unchanged (Fig. 3.5).

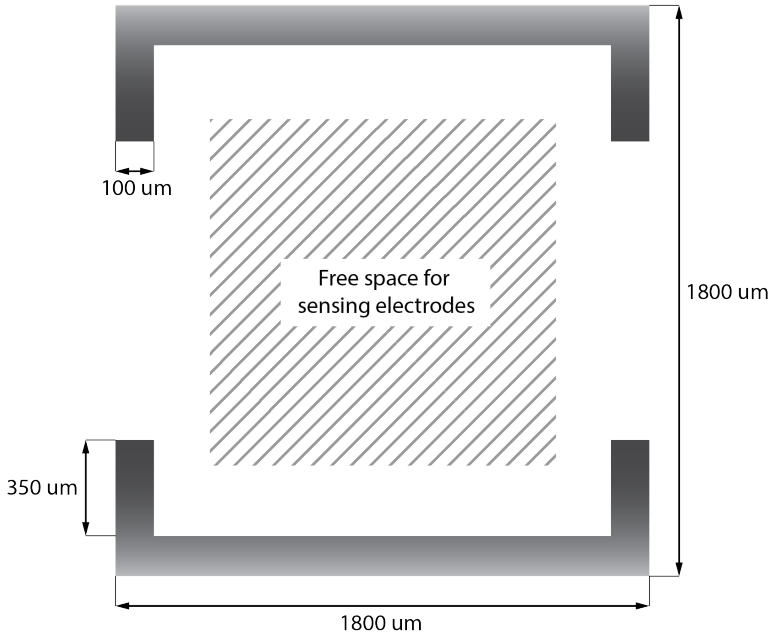

Figure 3.5: Common dimensions for each chip.

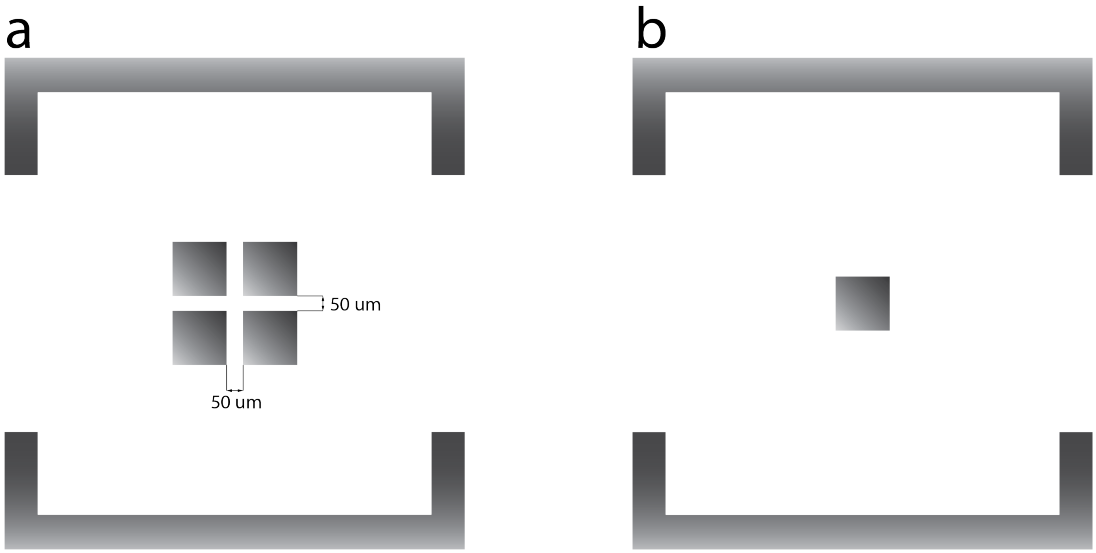

Figure 3.6: Sensing electrodes.

- **Four centered sensing electrodes and two external counter electrodes:** four sensing electrodes placed symmetrically with respect to the center of the well (Fig. 3.6a). Dimensions are 50×50 µm^2, 100×100 µm^2, and 200×200 µm^2. The measurement is performed between one sensing and one counter electrodes or one sensing and both counter electrodes.
- **Single centered electrode and two external counter electrodes:** here only one sensing electrode is designed, placed in the center of the well (Fig. 3.6b). Dimensions are 50×50 µm^2, 150×150 µm^2 and 250×250 µm^2. Measurement is performed between the sensing electrode and one counter electrodes or both counter electrodes.

The fist step for the fabrication has been the design of the masks, done in *Autodesk AutoCad 2016*. Chips are rectangular shaped and host 10 connection pads on each of the two short edges, more than the available pads on the PCB. The reason for testing an higher number of pads than the ones that actually can be connected to the PCB was to test the feasibility of this solution. In particular, as previously mentioned in the *Introduction* chapter, the future development of this simple test device will be the implementation of a much complex integrated CMOS postprocessing unit, combined with an array of multiplexed electrodes. Such a solution will require more connections than the ones needed for this simple test device. Having more I/O pads than the ones actually needed, some of them have been used as shorts to investigate the impedance of these connections. Dimensions of the chip are given in Table 3.1.

Two masks have been designed, one for the lift-off metal deposition and one for the openings in the passivating layer. Chips are fabricated starting from a 4" <100> p-type Silicon wafer. Two resists are spun (LOR3B-S1813) for better undercut control.

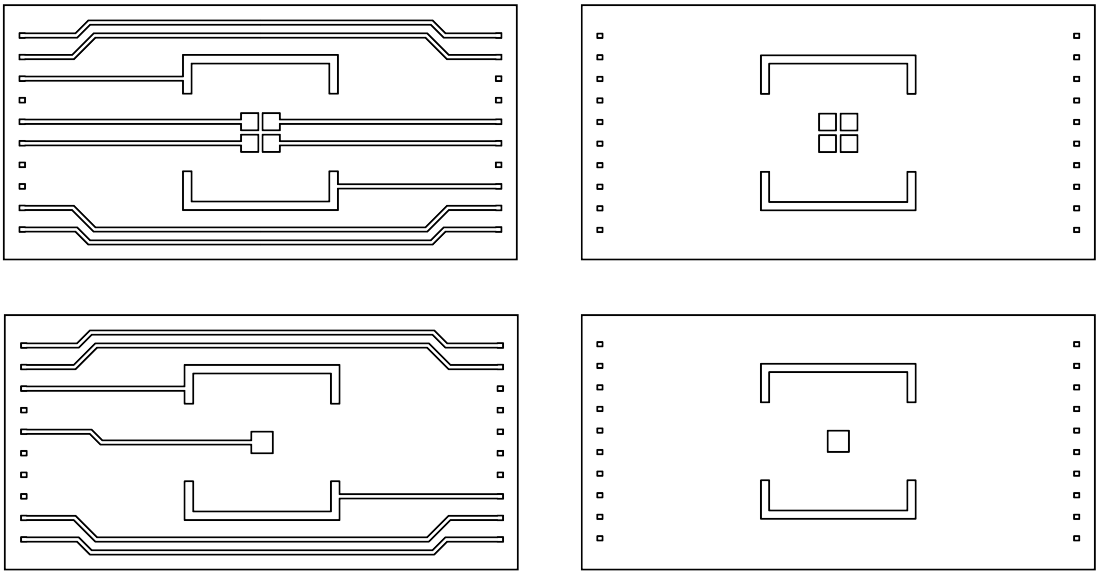

Figure 3.7: Masks for chips design, 4 sensing electrodes and single sensing electrode; on the left the mask for Pt deposition, on the right the mask for the openings in Si_3N_4 layer.

Table 3.1: Table of chip dimensions.

Dimension	**Value**
Chip area	6000×3000 µm^2
I/O pads area	65×55 µm^2
Counter electrode body area	1800×150 µm^2
Counter electrode arm area	350×150 µm^2
Sensing electrodes area (4-el.s)	50×50, 100×100, 200×200 µm^2
Sensing electrodes area (1-el.)	50×50, 150×150, 250×250 µm^2
Routes width	50 µm
Minimum pitch	150 µm

Main steps are the following, also shown in Figure 3.9a:

Si_3N_4 bottom insulating layer

1. Plasma cleaning: oxygen plasma for 20min at 360 W;
2. Si_3N_4 deposition: 500 nm of Si_3N_4 (PlasmaLab 80, *Oxford Instruments);*

Lift-off process

1. LOR3B positive resist: spin for 5s at 500rpm and then 45s at 3700rpm, followed by soft bake for 3min at 200°C;
2. S1813 positive resist: spin for 5s at 500rpm and then 45s at 3700rpm, followed by soft bake for 1min at 116°C;
3. Mask 1 exposure: Hg vapour lamp at I-line (365.4 nm wavelength) for 4s (135 mJ/cm^2) with hard contact (*Karl Suess* Mask Aligner);
4. Development: 60s in MF319;
5. Deposition: 20 nm of WTi (10%) followed by 200 nm Pt at 60°C (IonFab 300, *Oxford Instruments*);
6. Lift off: 4min in ultrasonic bath with Rem-400 solution, then rinsed in IPA;

Si_3N_4 passivating layer deposition

1. Plasma cleaning: oxygen plasma for 20min at 360 W;
2. Si_3N_4 deposition: 500 nm of Si_3N_4;
3. S1813 positive resist: spin for 5s at 500rpm and then 45s at 3700rpm, followed by soft bake for 1min at 116°C;
4. Mask 2 exposure: Hg vapour lamp at I-line (365.4 nm wavelength) for 4s (135 mJ/cm^2) with hard contact (*Karl Suess* Mask Aligner);

5. Development: 60s in MF319;
6. Plasma cleaning: oxygen plasma for 20min at 360 W;
7. Etching: 12min RIE (Plasmalab 100, *Oxford Instruments*);
8. Resist removal: 4min in ultrasonic bath with Rem-400 solution, then rinsed in IPA.

Dicing is done with a 200 µm saw.

3.3 Glass PCB

PCBs are fundamental components of each electronic setup. They are needed to drive signals between different electrical components, and also from sensors to readout systems. The latter is the case of the described device: signals to and from the electrodes contained in the silicon chips are driven through platinum routes towards the bigger connection pads. Since a transparent substrate could be beneficial for visual analysis, these routes are placed on a Borosilicate glass and passivated with Silicon Nitride.

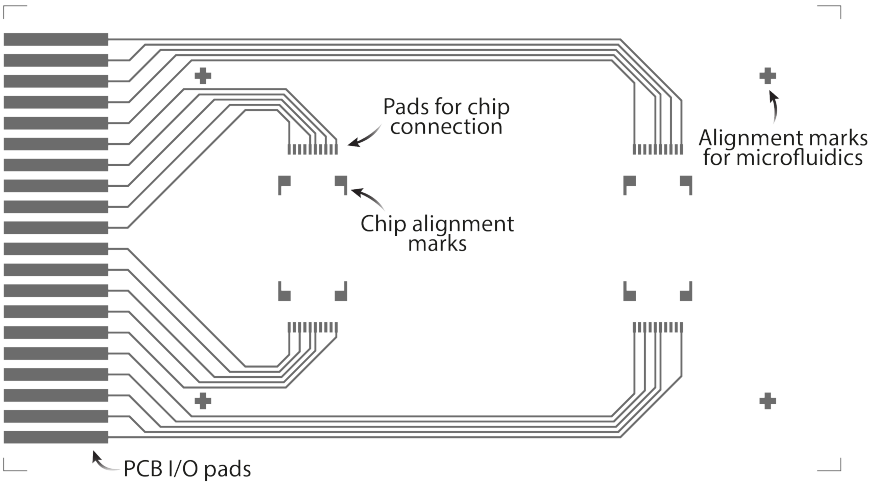

Figure 3.8: PCB layout.

Similarly to the chips, masks were drawn in *Autodesk AutoCAD 2016*. Dimensions for the glass slide and the PCB I/O pads are chosen in order to make the device compatible with an already available card reader. Each PCB provides 20 I/O connections, split between two chips which are placed in the center of the slide. All the dimensions are given in Table 3.2. Two masks have been designed, one necessary for the metal connections deposition and one for the openings in the dielectric passivating layer above them.

Table 3.2: Table of PCB dimensions.

Dimension	**Value**
Glass slide area	40.00×22.17 mm^2
I/O pads area	5000×610 μm^2
Wire bonding pads area	150×500 μm^2
Routes width	100 µm
Minimum pitch	250 µm

PCBs are microfabricated in clean-room starting from a 4" Borosilicate glass wafer, and the metal deposition is done through a lift-off lithographic process. Each wafer can fit 6 PCBs. Also in this case two resists are spun (LOR3B-S1813). Fabrication steps (Fig. 3.9b) are similar to the ones followed for the chips:

Lift-off process

1. LOR3B positive resist: spin for 5s at 500rpm and then 45s at 3700rpm, followed by soft bake for 3min at 200°C;
2. S1813 positive resist: spin for 5s at 500rpm and then 45s at 3700rpm, followed by soft bake for 1min at 116°C;
3. Mask 1 exposure: Hg vapour lamp at I-line (365.4 nm wavelength) for 4s (135 mJ/cm^2) with hard contact (*Karl Suess* Mask Aligner);
4. Development: 60s in MF319;
5. Deposition: 20 nm of WTi (10%) followed by 200 nm Pt at 60°C (IonFab 300, *Oxford Instruments*);

6. Lift off: 4min in ultrasonic bath with Rem-400 solution, then rinsed in IPA;

Si_3N_4 passivating layer deposition

1. Plasma cleaning: oxygen plasma for 20min at 360 W;
2. Si_3N_4 deposition: 500 nm of Silicon Nitride (PlasmaLab 80, *Oxford Instruments*);
3. S1813 positive resist: spin for 5s at 500rpm and then 45s at 3700rpm, followed by soft bake for 1min at 116°C;
4. Mask 2 exposure: Hg vapour lamp at I-line (365.4 nm wavelength) for 4s (135 mJ/cm^2) with hard contact;
5. Development: 60s in MF319;
6. Plasma cleaning: oxygen plasma for 20min at 360 W;
7. Etching: 12min RIE (Plasmalab 100, *Oxford Instruments*);
8. Resist removal: 4min in ultrasonic bath with Rem-400 solution, then rinsed in IPA.

At the end of the process, also in this case all the glass wafers are diced with a 200 µm saw.

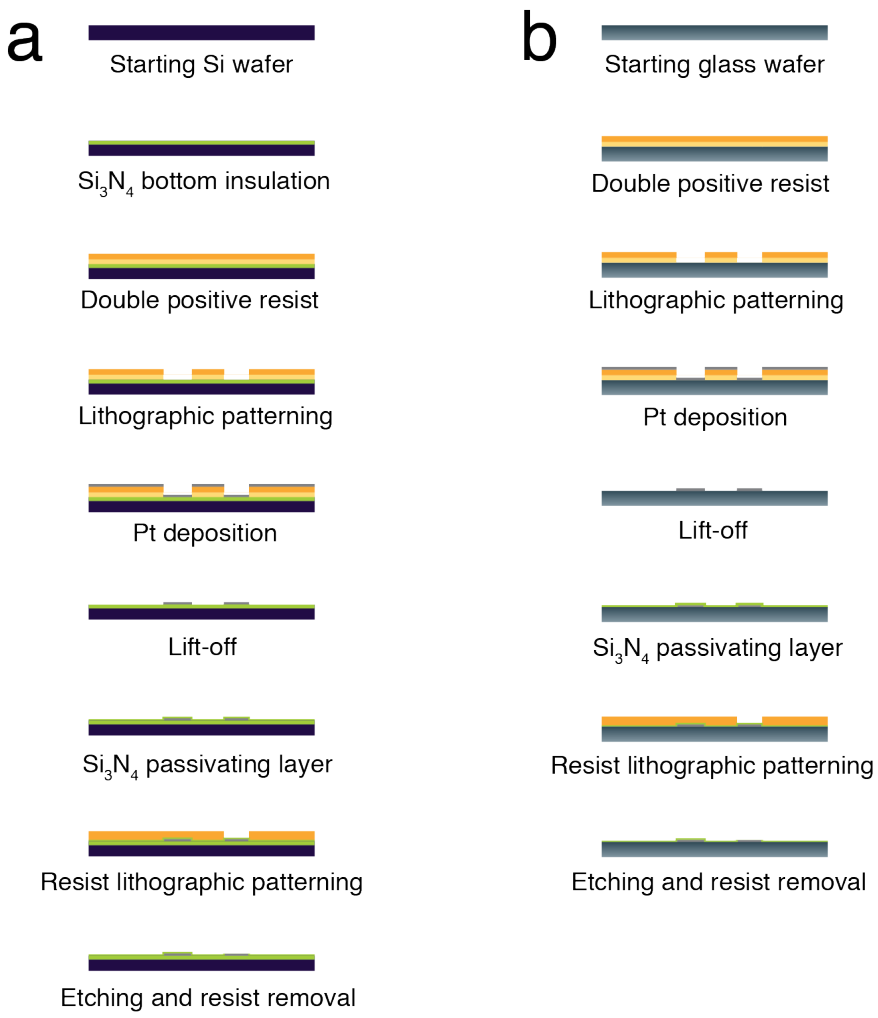

Figure 3.9: Scheme of the microfabrication process: a) chip fabrication, b) PCB fabrication, c) microfluidics fabrication.

3.4 Assembly

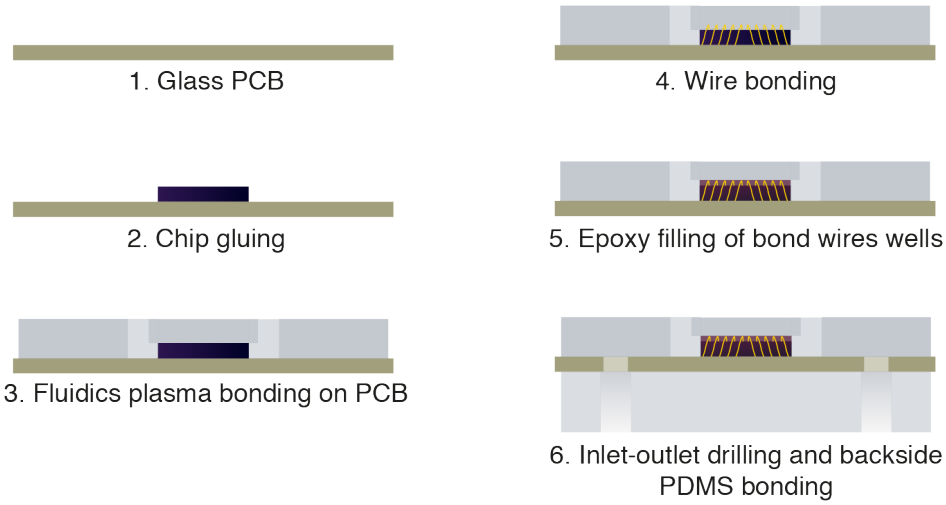

Figure 3.10: Device assembly steps for one chip.

A full scheme of the assembly process is shown in Fig. 3.10. First step for the process is gluing the chips onto the PCBs. This has been done using a two component epoxy glue (*EPO-TEK* H70E), then cured for 1 hour at 120°C (Fig. 3.12a). Subsequently, the PDMS fluidics is plasma bonded on the PCBs by activating both PDMS and PCB surfaces with plasma (30s at 50 W, 0.4 mbar O_2, *Diener Electronic*) and then putting them in contact. Plasma changes the chemical properties of both glass and PDMS surfaces and when they are put in contact a covalent bond occurs at the surfaces. This simple process guarantees a strong bond between PDMS and glass, but many agents can affect the goodness of the bonding. In particular, surfaces have to be clean and without oily footprints. To be sure no dirt is present both PDMS and glass are cleaned with soap and rinsed with distilled water before this process.

Moreover, the covalent bonding happens instantly as soon as the surfaces touch, so no correction of the alignment can be done afterwards, requiring then very high precision. This is obtained by a proper machine available in the laboratory, with very precise mechanical movement of x-y-z axes and angle of the substrate on which the PDMS is bonded.

The following step of this process is the wire bonding of the chips on the PCB, which is made with a semiautomatic bonding machine (*TPT HB16* wire bonder) operating in ball-ball ultrasonic bonding mode: small gold balls are placed on both PCB and chip pads, and connected with a 25 µm Au wire (Fig. 3.11). The ultrasonic bonding technology combines the effect of ultrasounds, heating and applied force to enhance the wire deformation on the pads. This technique consists in generating a ball from the wire with a small spark, sticking it on the first pad, pulling the wire and pressing it on the second pad (ball-wedge bonding). The reason why in this case balls are placed on both pads is that the latter ones are made of platinum instead of gold, then the adhesion is not strong enough to assure a reliable bonding with a ball-wedge technique. In fact, balls give a larger contact surface than just pressing the wire on the pad. Then, the wire is bonded to the second pad by sticking it on the previously placed gold balls, giving a stronger bond. These wires are then covered with epoxy (*EPO-TEK* 353ND) for protection, which is then cured for 12 hours at 80°C (Fig. 3.12b). Faster curing at higher temperature could lead to strong epoxy shrinkage that may affect the wire bonds.

Finally, inlets and outlets were added to the system to connect it to an external pump. With this goal, holes have been drilled into glass in the reservoir wells with a 800 µm diamond tip, specific for glass, rotating at 800rpm. A further PDMS layer (10:1 PDMS 2mm slice, cured 2 hours at 80°C then patterned with laser cutter) containing two 1 mm holes was then bonded on the back side of the PCB to seal the tube connections into the holes (Fig. 3.12.c).

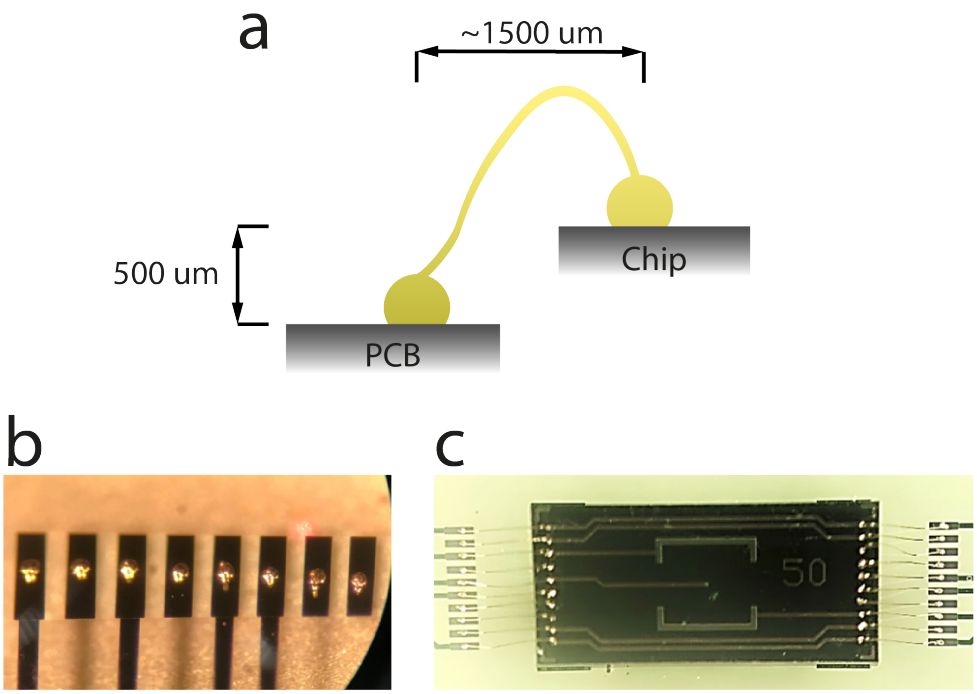

Figure 3.11: Ball-ball bonding: a) scheme of the bond, b) balls placed on PCB pads, c) wire bonds after the bonding process.

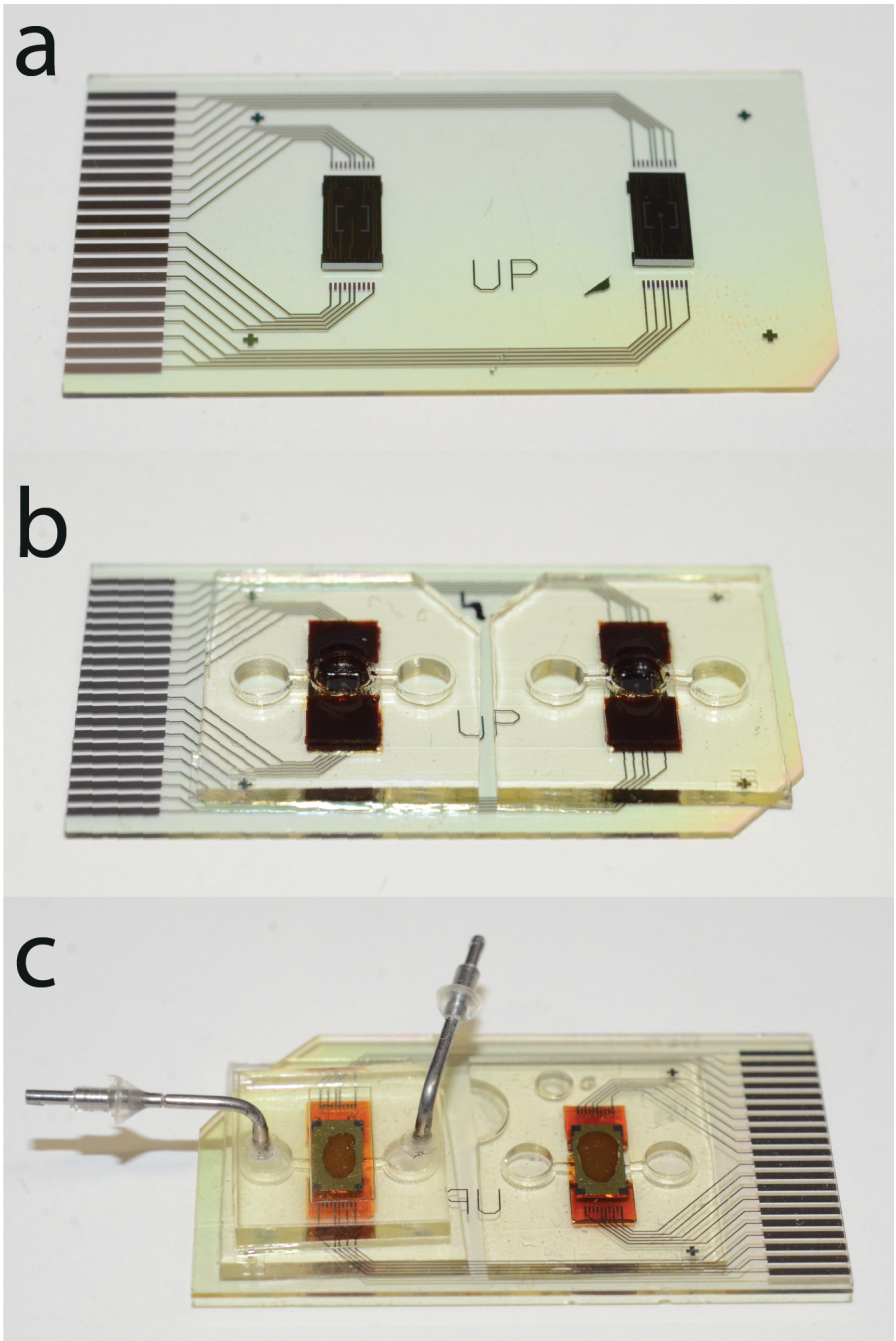

Figure 3.12: Device assembly: a) after chip gluing on the PCB, b) after microfluidics bonding, wire bonding and protection epoxy placement, c) after drilling holes into the glass PCB, backside PDMS bonding and inlet/outlet connection.

4

Experimental data

4.1 Loading and perfusion

The PDMS microfluidics loading is performed with constant inflow from both the tubes connections, while the chip is placed face down. Using a flow rate between 10-30 µl/min enables filling of the microfluidic network in ∼1-2 minutes. The medium injection is precisely controlled by an external syringe pump (neMESYS Syringes Pump, *CETONI Gmbh*). Two independently controlled glass syringes are connected to the device. For the connection, two metal 20GA 1/2" needles are used on both sides, linked to the main tube (PTFE 0.4×0.9 mm, S1810-06 *Bola Tubing*) through two larger junction tubes (0.76 mm ID Tygon LMT 55 *Idex, Ismatec*). During this process, liquid injected from the bottom of the two external wells tends to uniformly spread inside them. When its level reaches the one of the rims, it starts to follow the shape of a spherical cap. In the meanwhile, the channels putting in connection the three wells and the gravity force make the liquid level grow in the same proportion for each drop. Due to the intrinsic hydrophobicity of PDMS, a manual injection of medium in the channels is needed to establish the interconnections between the drops.

Furthermore, by knowing the amount of injected liquid the height of the drop can be analytically calculated:

$$\Delta V = \frac{1}{6}\pi h(3a^2 + h^2) \tag{4.1}$$

where ΔV is the difference between the initial and final volume, h is the drop

height from the top of the rim and a the radius of the well.

During the loading procedure both syringes work as inlets, but actually the advantage of this setup is the capability of establishing a continuous flow of medium. Inflow is handled by a 1 ml syringe, while outflow by a 0.5 ml for a more precise control. In particular, evaporation compensation is performed by varying the flow-rate of the outflow solution, so that to keep a stable drop height. Being the outflow syringe smaller, it is possible to trim the flow-rate with higher resolution.

4.2 Electronic readout system

The signals coming from the glass PCB are guided through a micro card reader and then given as input to a couple of analog multiplexers (ADG731, *Analog Devices*) placed on a custom designed PCB already used in the laboratory for similar setups. These two multiplexers are driven by an *Arduino Micro* controller: it has been programmed in order to read external commands from the serial connection to the PC, executed through an adapted *LabView* code, and actuate the multiplexers by writing as master on a 3 line serial interface. This is done through a SPI protocol at a frequency of 100 kHz by writing one byte on the serial line. Multiplexers store this byte in an input shift register, and select the related path according to a lookup table, working as analog demultiplexers. The muxed signals are given in output through two SMA connectors. Two SMA-BNC cables then connect this PCB to an external instrument (HF2LI, *Zurich Instruments*). This device operates as a lock-in amplifier, able to provide high resolution measurement from a high noise input. More in detail, the readout system required for the electrode sensing needs an applied signal on the counter electrodes, while the resulting current is collected from the sensing electrodes. This kind of measurements involve a massive amount of noise superimposed to the wanted signal, which needs to be filtered out. Then the role of the lock-in amplifier is to make a very narrow band-pass filter centered at the frequency of a reference signal, which in this case is the signal applied to the electrodes, thus virtually removing all the harmonics but the one of the wanted signal. To build a band-pass filter which follows the signal frequency, the recorded signal is multiplied by a reference one, generated by the same oscillator

of the injected signal, an operation that gives as result the sum and difference beats located at zero frequency and at $2f_{signal}$; with this operation the wanted signal is moved to baseband, and can be sent through a steep low-pass filter to filter out all the noise (Fig. 4.1). Also, to keep the sensing electrode at 0 V and convert the collected current into a voltage signal, the input signal is sent through a transimpedance amplifier with feedback resistance Z = 1 kΩ (Fig. 4.2).

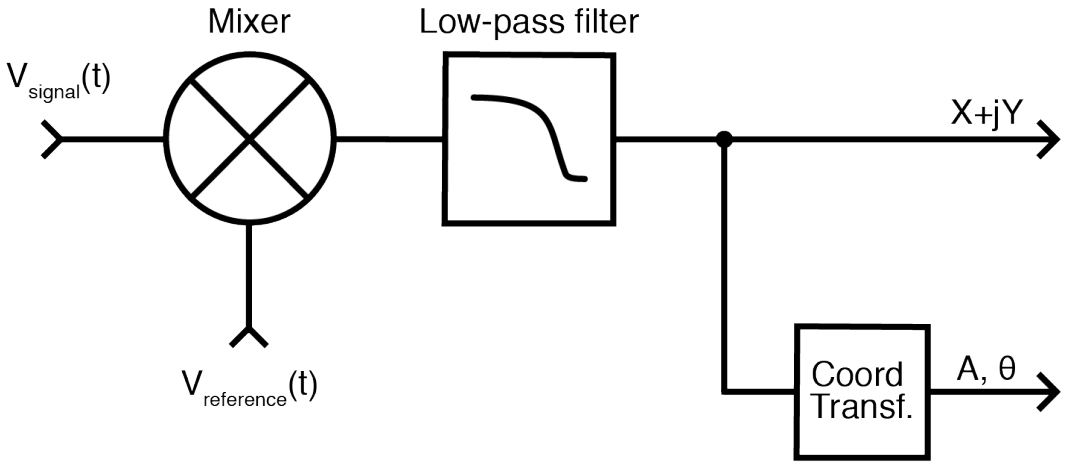

Figure 4.1: Principle scheme of a generic Lock-in filter.

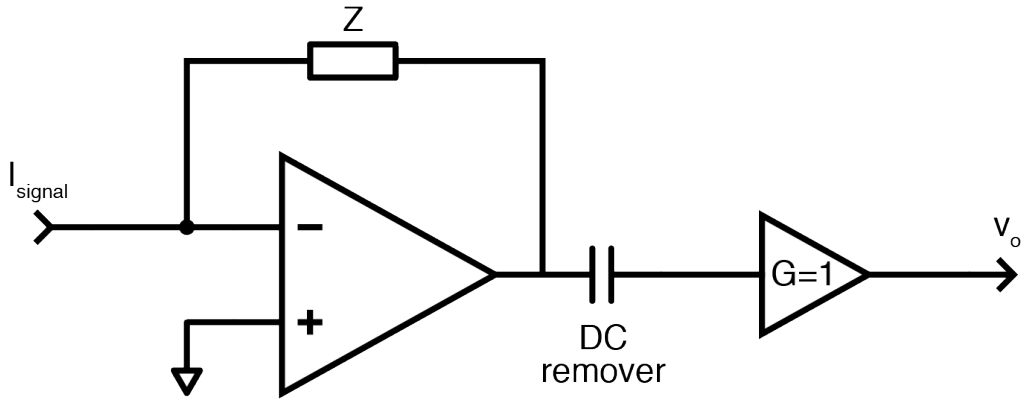

Figure 4.2: Scheme of a transimpedance amplifier circuit.

4.3 Microscope setup

During the experiments, imaging is done using an inverted microscope (*NIKON Ti Eclipse*), with 4× and 10× magnification objectives, and a CFI fluorescence light engine (*Lumenscore Spectra X*). The advantages of using an inverted microscope combined with bottom illumination is the capability of imaging the central well, on top of which the silicon chip is placed. With this technique it is possible to image the content of the well responsible for the electrical sensing, thus check the correct placement of the sample while running the experiment. Since the fluorescence lamp is used in broadband mode, its intensity was set to 2%. Furthermore, the surrounding atmosphere is maintained in an incubation box with gas mixing (*The Brick, Life Imaging Services*) and temperature (*The Cube, Life Imaging Services*) controllers, set at 95% humidity, 5% CO_2 and 37°C.

Thanks to the high-precision motorized focus z-stage the distances between the different heights of the microfluidic system can be measured. This simple process is based on focusing on different features such as the bottom of the well, the electrodes, the top of the rim or the sample and record the related positions of the z-stage, given with sub-µm resolution. Imaging is acquired through an high sensitivity camera (*ORCA-Flash4.0 V3* Digital CMOS camera), with an exposure ranging between 15 and 50 ms depending on the selected magnification.

The control of microscope stage position, light intensity and flow rates for the syringe pumps are done through an open-source software for microscope control (*Youscope R2017*), which lets the user add any supported peripheral device and set up automated controls (Lang M., 2012). For example, an automated compensation of the evaporation, which has already been minimized by the high humidity atmosphere in the chamber, can be set up combining an autofocusing process on the sample with a self-learning algorithm which trims the medium flow rate. The software looks for the current z-stage position which focuses on the sample with an autocorrelation algorithm, compares it to the one measured previously and based on this measurement actuates the syringe pump updating the flow rate, raising it in case the sample moves upwards and vice versa. In addition, having two active syringe pumps respectively connected to the two tube connections of the chip

allows to set a continuous perfusion flow by simultaneously injecting and removing medium. In this case the evaporation compensation is done by adjusting the flow-rate of the outflow syringe while keeping a steady inflow.

4.4 Stability of medium conductivity

Medium conductivity plays an important role in the measurement when doing EIS. The effects of conductivity variation could potentially affect the goodness of the measurement, since what is actually under measure is the impedance increase or decrease with the spheroid size. Therefore, any unwanted fluctuation of the ion concentration in the medium has to be avoided. With this goal, the device was filled with PBS and kept under constant flow of 0.3 µl/min to continuously refresh the medium in the microfluidics, while evaporation was automatically corrected by trimming the inflow syringe control. Since the autofocusing system requires an object to focus on, a ∼600 µm glass bead was placed in one of the two lateral wells. In the meanwhile, a 100 mV_{PP} signal at 100 kHz is applied and the current simultaneously recorded between two sensing electrodes (a 4-sensing chip was used, with 50×50 μm^2 sensing electrodes). By doing the measure between two close electrodes, the electric field hardly spreads far from the electrodes plane, then the current variations due to the drop height should be minimized. Current is then converted into a voltage measurement through the previously described amplifier circuit. By knowing the transimpedance gain the conductance related to the detected voltage is computed. Results are given in Fig. 4.3. Here the wanted drop height, measured from top of the rim, is set to 300 µm, which corresponds to the 0 value of the observed drop height offset. Negative values represent bigger drops (i.e. larger drop height), and vice versa. How it can be seen, at first the drop height was larger than the wanted one, then the system lowered the inflow and slowly reduced the size of the drop. This caused a slight lowering of the collected current, which settled to a stable value after ∼90 min. For the remaining part of the experiment the recorded voltage was constant, hence also the conductivity. Concerning the measurement error of the electric readout system, it was computed as standard deviation over 1 s in condition of constant impedance for the sample,

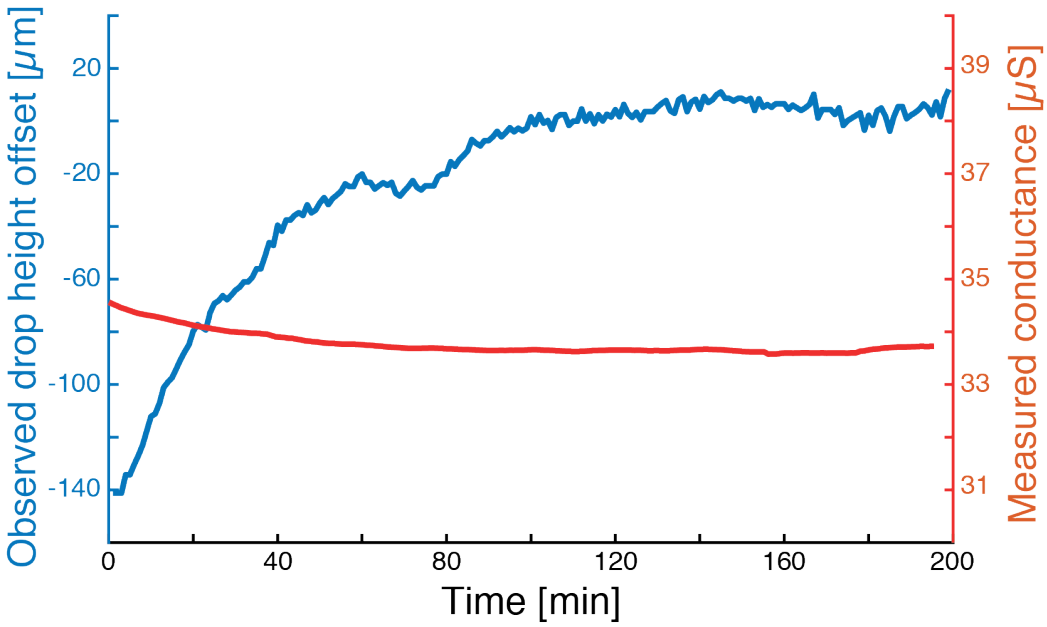

Figure 4.3: Stability of the PBS conductivity over time; output with 100 mV_{PP}, 100 kHz applied signal, 0.3 µl/min continuous perfusion with automatic compensation of evaporation.

at a sampling speed of 229.4 Hz. The calculated standard deviation is 0.1 µV when the measured voltage amplitude is 3.4 mV, then the relative error is 0.0033%. The measurement incertitude is then mostly related to the transimpedance gain tolerance, quantified in 1%. Differently for the autofocus evaluation of the drop height offset, the standard deviation was computed over 30 min of stable drop, giving a value of 3 µm. This error is related to the different plane on which the algorithm selects the best focus score, and can fluctuate in the range of some microns. Since in this experiment high accuracy in the evaluation of the drop is not required, but only an estimation of its height for the evaporation compensation, such a precision is enough for what is presented.

4.5 Sensitivity and electrode-sample distance

The effect of field lines blocking and bending due to the growing spheroid is connected to the electrode-sample distance. As it can be seen from simulations (Fig. 2.3), the impedance increase is consequent to the reduced conductive region close to the sensing electrodes, which is also the region where most of the voltage drop in the medium is placed. Then by putting a large glass bead in the main well and slowly bringing it closer to the electrodes by reducing the drop size, the optimal distance between the spheroid and the sensing electrodes can be investigated. Therefore, in this experiment a glass bead was put in the central well. Its diameter was precisely measured by taking a picture while focusing on its edge, then converting pixels to micrometers; the real diameter of the spheroid was found to be 1000 µm. To know the actual distance between the bead and the sensing electrodes also the depth of the central well was measured, from the plane containing the electrodes up to the top of the rim. Unexpectedly, it was found to be 600 µm instead of 800 µm as it was designed to be. This event is probably related to an over shrinking of the PDMS during the casting process, due to the weight put on top of the two molds while curing to ensure the sealing between them. Other dimensions such as well diameter were found to be correct.

After filling the microfluidics with PBS and putting the bead in the main well, drop height was brought at 900 µm from the top of the rim (then 1500 µm from the plane of the electrodes). As previously mentioned, by exploiting the backside illumination with an inverted microscope it is possible to see the content of the central well, thus to focus on the bead itself. From this starting point, medium is then removed by setting an inflow of 1 µl/min and an outflow of −2 µl/min. By knowing the starting height of the drop and the flow rate is then possible to relate its size at any given time by inverting the formula in Eq. 4.1:

$$\frac{\pi}{6}h^3 + \frac{\pi}{2}a^2h + V_{initial} - V_{removed} = 0 \tag{4.2}$$

and then solving the polynomial equation in h[1], selecting the real root for any

[1]Recalling that a is the radius of the well, h the drop height, $V_{initial}$ the starting volume and $V_{removed}$ the total volume removed by the constant outflow updated at each time.

case. These drop heights are then related to the sensed voltage, since reducing the drop size brings the bead closer to the electrodes: drop height can be related to the bead-electrodes distance by observing that:

$$d_{el-bead} = l_{well} + h - d_{bead} \tag{4.3}$$

where l_{well} is the well depth, h the drop height and d_{bead} the bead diameter. Also in this case a chip with 4-sensing electrodes is used (150×150 µm^2). The signal is a 100 mV_{PP} sinewave swept over a wide frequency range between 1 kHz and 3 MHz and is applied to one of the counter electrodes, while the resulting current is collected from one of the two sensing electrodes on the opposite side.

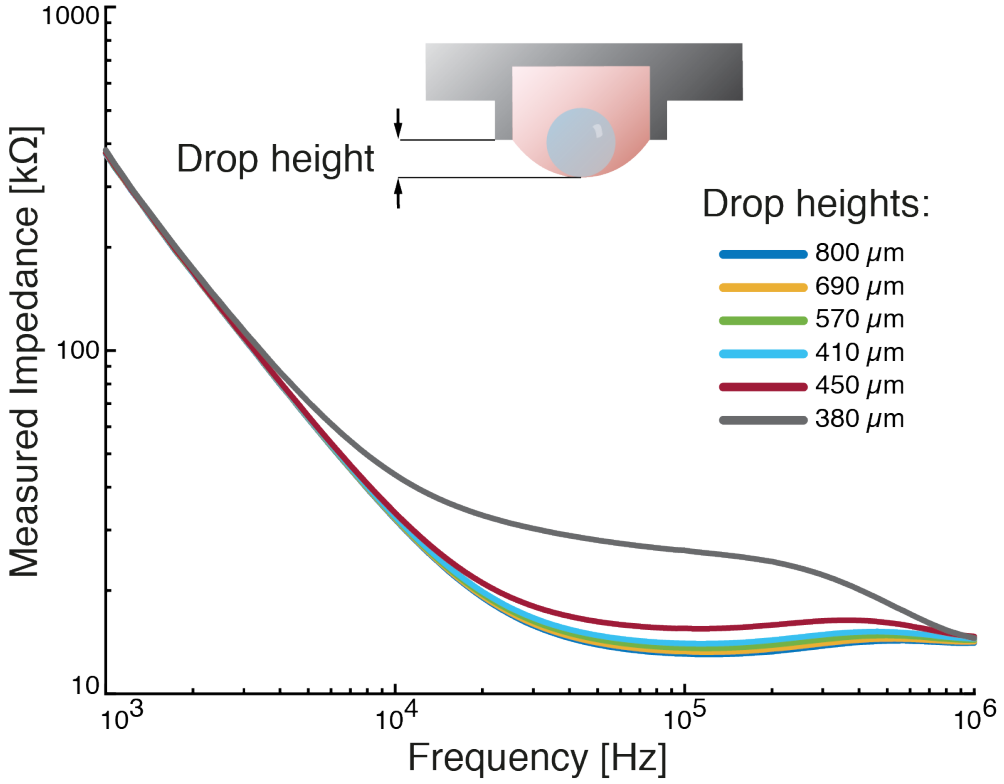

Figure 4.4: Measured voltages w.r.t. drop height in PBS and 1000 µm glass bead; output with 100 mV_{PP} applied signal swept from 1 kHz to 3 MHz, -1 µl/min continuous flow. Bead-electrodes distance can be obtained recalling that $d_{el-bead} = h - 400$ µm.

Results are shown in Fig. 4.4. Here it can be seen how at low frequency the presence of the double layer capacitance cuts out any bead-related impedance variation. Then, as expected from simulations, a variation in the measured voltage is obtained with the bead getting closer to the electrodes. The maximum sensitivity is located at around 100-200kHz. Then for higher frequency another effect due to parasitic capacitances is shown, probably related to the coupling between the lines on the PCBs. Most of the bead-related impedance increase is visible when drop height is lower than 450 µm, which is linked to an electrodes-bead distance lower than 50 µm.

To better investigate the variation at a target frequency, these results are then analyzed as relative variations at a fixed frequency of 100 kHz (Fig. 4.5). In this

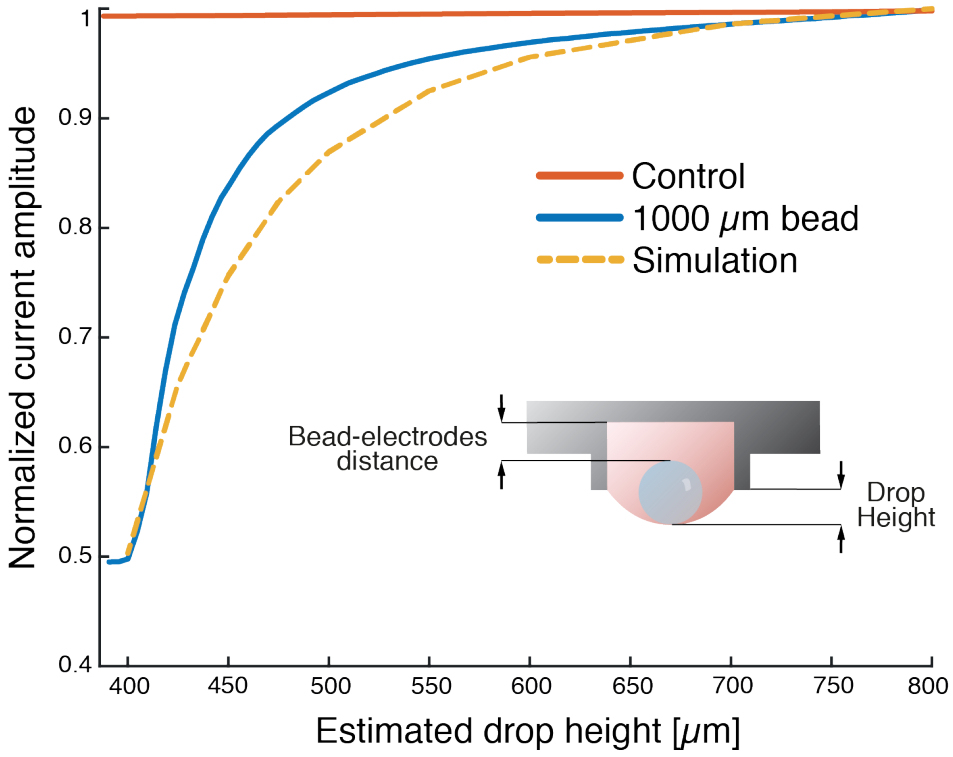

Figure 4.5: Normalized current w.r.t. estimated drop height in PBS and 1000 µm glass bead; output with 100 mV_{PP}, 100 kHz applied signal, -1 µl/min continuous flow. Bead-electrodes distance can be obtained recalling that $d_{el-bead} = h - 400$ µm.

figure a control line is given too, measured repeating the experiment with no bead

in the central well; as previously outlined, the conductivity can be kept stable with a continuous perfusion, while variations in current due to drop height are found to be very small if compared to bead-related ones. With the drop height getting smaller, the sensed current lowers and at a drop height of 480 µm the difference from the control line is 10%. From a first computation, it was found that the bead hits the electrodes plane already with a 500 µm drop height, where the current lowering suddenly stops. Being the well depth 600 µm measured from the chip to the top of the rim, and being the bead diameter 1000 µm, the drop height at which the bead hits the electrodes is expected to be 400 µm. This result is probably due to tolerances in measuring the glass bead radius, since it is not a perfect sphere, and neglecting drop deformation due to gravity especially when its size is large, which gives an overestimation of the initial drop volume. For a better representation of the results, drop height is estimated starting from the value at which the bead hits the electrodes, which is 400 µm, and then all the other heights are computed. A strong reduction in current is measured when the distance between the bead and the electrodes is lower than 150-200 µm. Furthermore, this result can be compared to the one obtained through simulations of the previously described model, adapted for these dimensions. The current decrease due to the bead touching the electrodes is verified, while the trend shows a slightly lower sensitivity in the real measurement with respect to the simulations, where the signal drop starts at higher drop heights. This might be linked to a minor spread of the voltage drop in the electrolyte close to the sensing electrode, due to different conductivity in the model and in the real medium. Nevertheless, simulation results should be intended as ideal, while many non-idealities may occur in real experiments such as non centering of the spheroid, slight differences in the medium ions concentration or in the dimensions of the electrodes. Since the recording in the frequency sweep is done through averaging over multiple measures, a standard deviation can be calculated for each recorded point. By considering the maximum of these points the measurement error for the voltage measure is found to be 45 µV for high frequencies over 300 kHz and 10 µV under 200kHz. With this standard deviation evaluation, also in this case the relative error of the data in Figure 4.4 can be estimated to be mostly related to the tolerance in the transimpedance amplifier gain, which is 1%. When the normalized amplitude is shown (Fig. 4.5 the error related to the amplifier gain is removed and the incertitude can be quantified with the previously described

standard deviation, then less than 1%. For the focusing-based measure of the first distance, being the precision of the piezoelectric actuator of the z-stage 0.01 µm, the measurement error can be considered to be the incertitude in the selected focus plane, which in all cases is less than ∼10 µm.

5

Discussion

The results and experimental proofs that have been obtained during this project show the feasibility of integrating MEA chips with microfluidics hanging-drop networks. The latter brings the benefits in cell culturing widely described before, but the simple integration with an electronic readout system opens many valuable strategies in data extraction from multicellular microtissues. This work is mainly focused on the fabrication of the device and the application of EIS for spheroid size sensing, but this is not the only possible application for these electrodes arrays. By flipping the device upside-down, the microtissue can be easily brought in contact to the electrodes, enabling cell stimulation or tissue characterization through EIS. Furthermore, functionalized electrodes can provide real time monitoring of the concentration for several species in the medium, which combined to EIS detection of tissue size would give a consistent dataset to monitor the culturing process. This would bring huge advantages when it comes to cell-based assays.

Starting from simulations, which also have been proven to provide a reliable reproduction of what has been observed during the experiments, optimal dimensions for the required sensing approach can be obtained. These quantities mainly depend on the depth of the well containing the main drop. A noteworthy result from the computed model is the effectively achievable sensitivity to tissue size variation, obtained when the spheroid-electrode distance is lower than $\sim$200 µm. This "rule of thumb" was also verified during the experiments.

Moreover, even if the microfabrication process raised several challenges to be overcome such as the necessity of an hydrophobic rim, the thin PDMS layer casting difficulties, the gold wire bonding on platinum pads and the epoxy curing step, the

final goal of proving its feasibility has been achieved. Particular attention has to be paid to the material the molds are made with, since surface roughness terribly lowers the success rate for the PDMS casting and detaching step. Furthermore, a complete etching of the Silicon Nitride passivating layer on the Platinum pads must be obtained, otherwise even a nanometric covering can compromise the yield of the wiring bonds.

The experimental data obtained on one of the produced devices also showed a good stability of the hanging drop system over hours. The capability of keeping under control the ion concentration in the medium has been obtained by limiting the evaporation rate with an high humidity environment and continuously perfusing new liquid. This was one of the main concerns when looking at the expected sensitivity in the simulation results, since non tissue-related conductivity variations can not be filtered out from the measured current with the current electrodes. Moreover, the presence of the rim enlarges the tissue-electrodes minimum distance, dramatically lowering the sensitivity. Since microtissue spheroids are commonly cultured up with diameters ranging between ∼200-500µm, the distance between electrodes and top of the rim should be reduced in order to bring them closer to the electrodes.

6

Conclusion and Outlook

The integration of MEAs with hanging-drop networks combines the advantages of a fully characterized open microfluidic platform, which allows easy formation and culturing of multicellular spheroids, with an electronic readout system capable of providing a real time monitoring of the sample. This microfluidic network not only enhances the previously developed electronics with an advantageous culturing platform, but enables the study of heterogeneous interacting microtissues connected together according to their physiology. Here, many different biologically relevant quantities can be constantly monitored through EIS or properly functionalized electrodes, or even a direct electrical stimulation and record of the sample can be realized by flipping the device upside-down.

EIS can be efficiently simulated with a Finite Element Model, exploited to compute the optimal dimensions for the well. The results, being validated by the experimental data, offer a reliable support for the design step avoiding a trial and error progress during fabrication, thus helping in saving time and resources. Moreover, the microfabrication process for this test device only involves very common and well known techniques such as low pressure and plasma enhanced chemical vapor deposition, photolithographic patterning and PDMS casting, with confirmed high yield and reproducibility.

Therefore, the designed device represents a suitable and reproducible approach for merging electrical sensing and microfluidic open networks, which could be applied in the future development of this promising technology.

Bibliography

F. A. Alexander, D. T. Price, and S. Bhansali. From Cellular Cultures to Cellular Spheroids: Is Impedance Spectroscopy a Viable Tool for Monitoring Multicellular Spheroid (MCS) Drug Models? *IEEE Reviews in Biomedical Engineering*, 6:63–76, 2013. ISSN 1937-3333. doi: 10.1109/RBME.2012.2222023. URL http://ieeexplore.ieee.org/document/6319364/.

P. Bertemes-Filho. Electrical Impedance Spectroscopy. In *Bioimpedance in Biomedical Applications and Research*, pages 5–27. Springer International Publishing, Cham, 2018. doi: 10.1007/978-3-319-74388-2_2. URL http://link.springer.com/10.1007/978-3-319-74388-2{_}2.

M. J. Bissell, H. Hall, and G. Parry. How does the extracellular matrix direct gene expression? *Journal of Theoretical Biology*, 99(1):31–68, nov 1982. ISSN 0022-5193. doi: 10.1016/0022-5193(82)90388-5. URL https://www.sciencedirect.com/science/article/pii/0022519382903885?via{%}3Dihub.

S. C. Burgel, Y. Schmid, I. Agarkova, D. A. Fluri, J. M. Kelm, A. Hierlemann, and O. Frey. Simultaneous impedance spectroscopy and stimulation of human iPS-derived cardiac 3D spheroids in hanging-drop networks. *Proceedings of the IEEE International Conference on Micro Electro Mechanical Systems (MEMS)*, 2015-Febru(February):226–229, 2015. ISSN 10846999. doi: 10.1109/MEMSYS.2015.7050928.

S. C. Bürgel, L. Diener, O. Frey, J.-Y. Kim, and A. Hierlemann. Automated, Multiplexed Electrical Impedance Spectroscopy Platform for Continuous Monitoring of Microtissue Spheroids. *Analytical Chemistry*, 88(22):10876–10883, 2016. ISSN 0003-2700. doi: 10.1021/acs.analchem.6b01410. URL http://pubs.acs.org/doi/abs/10.1021/acs.analchem.6b01410.

T. Chi, J. S. Park, J. C. Butts, T. A. Hookway, A. Su, C. Zhu, M. P. Styczynski, T. C. McDevitt, and H. Wang. A Multi-Modality CMOS Sensor Array for Cell-Based Assay and Drug Screening. *IEEE Transactions on Biomedical Circuits*

and Systems, 9(6):801–814, dec 2015. ISSN 1932-4545. doi: 10.1109/TBCAS.2015.2504984. URL http://ieeexplore.ieee.org/document/7390111/.

K. S. Cole and R. H. Cole. Dispersion and absorption in dielectrics I. Alternating current characteristics. *The Journal of Chemical Physics*, 9(4):341–351, apr 1941. ISSN 00219606. doi: 10.1063/1.1750906. URL http://aip.scitation.org/doi/10.1063/1.1750906.

J. Dragas, V. Viswam, A. Shadmani, Y. Chen, R. Bounik, A. Stettler, M. Radivojevic, S. Geissler, M. E. J. Obien, J. Muller, and A. Hierlemann. In Vitro Multi-Functional Microelectrode Array Featuring 59 760 Electrodes, 2048 Electrophysiology Channels, Stimulation, Impedance Measurement, and Neurotransmitter Detection Channels. *IEEE Journal of Solid-State Circuits*, 52(6):1576–1590, jun 2017. ISSN 0018-9200. doi: 10.1109/JSSC.2017.2686580. URL http://ieeexplore.ieee.org/document/7913669/.

M. Eiraku, K. Watanabe, M. Matsuo-Takasaki, M. Kawada, S. Yonemura, M. Matsumura, T. Wataya, A. Nishiyama, K. Muguruma, and Y. Sasai. Self-Organized Formation of Polarized Cortical Tissues from ESCs and Its Active Manipulation by Extrinsic Signals. *Cell Stem Cell*, 3(5):519–532, 2008. ISSN 19345909. doi: 10.1016/j.stem.2008.09.002.

M. Eiraku, N. Takata, H. Ishibashi, M. Kawada, E. Sakakura, S. Okuda, K. Sekiguchi, T. Adachi, and Y. Sasai. Self-organizing optic-cup morphogenesis in three-dimensional culture. *Nature*, 472(7341):51–56, apr 2011. ISSN 0028-0836. doi: 10.1038/nature09941. URL http://www.nature.com/articles/nature09941.

O. Frey, P. M. Misun, D. A. Fluri, J. G. Hengstler, and A. Hierlemann. Reconfigurable microfluidic hanging drop network for multi-tissue interaction and analysis. *Nature Communications*, 5, 2014. doi: 10.1038/ncomms5250. URL https://www.nature.com/articles/ncomms5250.pdf.

G. W. Gross, B. K. Rhoades, H. M. Azzazy, and Ming-Chi Wu. The use of neuronal networks on multielectrode arrays as biosensors. *Biosensors and Bioelectronics*, 10(6-7):553–567, jan 1995. ISSN 09565663. doi: 10.1016/0956-5663(95)

96931-N. URL https://www.sciencedirect.com/science/article/pii/095656639596931N.

J. Guo, W. Ng, J. Yuan, S. Li, and M. Chan. A 200-Channel Area-Power-Efficient Chemical and Electrical Dual-Mode Acquisition IC for the Study of Neurodegenerative Diseases. *IEEE Transactions on Biomedical Circuits and Systems*, 10(3):567–578, jun 2016. ISSN 19324545. doi: 10.1109/TBCAS.2015.2468052. URL http://ieeexplore.ieee.org/document/7310874/.

N. Haandbæk, S. C. Bürgel, F. Heer, and A. Hierlemann. Characterization of subcellular morphology of single yeast cells using high frequency microfluidic impedance cytometer. *Lab Chip*, 14(2):369–377, dec 2014. ISSN 1473-0197. doi: 10.1039/C3LC50866H. URL http://xlink.rsc.org/?DOI=C3LC50866H.

A. Héduit, I. Quinio, D. Stadmuller, and D. Thévenot. Modified platinum electrodes: electrochemical characteristics and behaviour in activated sludge. *Water Science and Technology*, 34:143–150, 1996.

A. Y. Hsiao, Y.-C. Tung, C.-H. Kuo, B. Mosadegh, R. Bedenis, K. J. Pienta, and S. Takayama. Micro-ring structures stabilize microdroplets to enable long term spheroid culture in 384 hanging drop array plates. *Biomedical microdevices*, 14 (2):313–23, apr 2012. ISSN 1572-8781. doi: 10.1007/s10544-011-9608-5. URL http://www.ncbi.nlm.nih.gov/pubmed/22057945http://www.pubmedcentral.nih.gov/articlerender.fcgi?artid=PMC3304008.

J. M. Jukes, S. K. Both, A. Leusink, L. M. T. Sterk, C. A. van Blitterswijk, and J. de Boer. Endochondral bone tissue engineering using embryonic stem cells. *Proceedings of the National Academy of Sciences*, 105(19):6840–6845, may 2008. ISSN 0027-8424. doi: 10.1073/pnas.0711662105. URL http://www.pnas.org/cgi/doi/10.1073/pnas.0711662105.

I. Kehat, D. Kenyagin-Karsenti, M. Snir, H. Segev, M. Amit, A. Gepstein, E. Livne, O. Binah, J. Itskovitz-Eldor, and L. Gepstein. Human embryonic stem cells can differentiate into myocytes with structural and functional properties of cardiomyocytes. *Journal of Clinical Investigation*, 108(3):407–414, aug 2001. ISSN 0021-9738. doi: 10.1172/JCI12131. URL http://www.jci.org/articles/view/12131.

S. J. Lang M., Rudolf F. Use of YouScope to Implement Systematic Microscopy Protocols. *Current Protocols in Molecular Biology*, pages 14—-21, 2012. URL http://langmo.github.io/youscope/.

N. Lumelsky. Differentiation of Embryonic Stem Cells to Insulin-Secreting Structures Similar to Pancreatic Islets. *Science*, 292(5520):1389–1394, may 2001. ISSN 00368075. doi: 10.1126/science.1058866. URL http://www.sciencemag.org/cgi/doi/10.1126/science.1058866.

P. M. Misun, A. Shadmani, A. Hierlemann, and O. Frey. Integrating multi-electrode arrays in microfluidic hanging-drop networks. *Proceedings of the IEEE International Conference on Micro Electro Mechanical Systems (MEMS)*, pages 91–94, 2017. ISSN 10846999. doi: 10.1109/MEMSYS.2017.7863347.

F. Pampaloni, E. G. Reynaud, and E. H. K. Stelzer. The third dimension bridges the gap between cell culture and live tissue. *Nature Reviews Molecular Cell Biology*, 8(10):839–845, oct 2007. ISSN 1471-0072. doi: 10.1038/nrm2236. URL http://www.nature.com/articles/nrm2236.

R. Pethig. Dielectric properties of body tissues. *Clinical Physics and Physiological Measurement*, 8(4A):5–12, nov 1987. ISSN 0143-0815. doi: 10.1088/0143-0815/8/4A/002. URL http://stacks.iop.org/0143-0815/8/i=4A/a=002?key=crossref.1ca025db1676c2ec8818d92fafa83d79.

M. Ravi, V. Paramesh, S. R. Kaviya, E. Anuradha, and F. D. Paul Solomon. 3D cell culture systems: Advantages and applications. *Journal of Cellular Physiology*, 230(1):16–26, jan 2015. ISSN 10974652. doi: 10.1002/jcp.24683. URL http://doi.wiley.com/10.1002/jcp.24683.

Y. R. Schmid, S. C. Bürgel, P. M. Misun, A. Hierlemann, and O. Frey. Electrical Impedance Spectroscopy for Microtissue Spheroid Analysis in Hanging-Drop Networks. *ACS Sensors*, 1(8):1028–1035, 2016. ISSN 23793694. doi: 10.1021/acssensors.6b00272.

H. P. Schwan and C. F. Kay. The Conductivity of Living Tissues. *Annals of the New York Academy of Sciences*, 65(6):1007–1013, 1957. ISSN 17496632. doi: 10.1111/j.1749-6632.1957.tb36701.x.

A. Stett, U. Egert, E. Guenther, F. Hofmann, T. Meyer, W. Nisch, and H. Haemmerle. Biological application of microelectrode arrays in drug discovery and basic research, oct 2003. ISSN 16182642. URL http://www.ncbi.nlm.nih.gov/pubmed/12923608http://link.springer.com/10.1007/s00216-003-2149-x.

H. Suga, T. Kadoshima, M. Minaguchi, M. Ohgushi, M. Soen, T. Nakano, N. Takata, T. Wataya, K. Muguruma, H. Miyoshi, S. Yonemura, Y. Oiso, and Y. Sasai. Self-formation of functional adenohypophysis in three-dimensional culture. *Nature*, 480(7375):57–62, nov 2011. ISSN 0028-0836. doi: 10.1038/nature10637. URL http://www.nature.com/doifinder/10.1038/nature10637.

Z. Zhu, O. Frey, D. S. Ottoz, F. Rudolf, and A. Hierlemann. Microfluidic single-cell cultivation chip with controllable immobilization and selective release of yeast cells. *Lab Chip*, 12(5):906–915, feb 2012. ISSN 1473-0197. doi: 10.1039/C2LC20911J. URL http://xlink.rsc.org/?DOI=C2LC20911J.